https://doi.org/10.1016/j.ensm.2023.103056

Facile Anion Engineering: A Pathway to Realizing Enhanced Triple Conductivity in Oxygen Electrodes for Reversible Protonic Ceramic Electrochemical Cells

Xi Chen[a], Na Yu[a], Idris Temitope Bello[a], Daqin Guan[a], Zheng Li[a], Tong Liu[a], Tong Liu[b], Zongping Shao[c], Meng Ni[a]*

[a] Department of Building and Real Estate, Research Institute for Sustainable Urban Development (RISUD) and Research Institute for Smart Energy (RISE), The Hong Kong Polytechnic University, Hung Hom, Kowloon, Hong Kong, China

[b] Key Laboratory of Green Chemical Process of Ministry of Education, Key Laboratory of Novel Reactor and Green Chemical Technology of Hubei Province, School of Chemical Engineering and Pharmacy, Wuhan Institute of Technology, Wuhan 430205, P. R. China

[c] WA School of Mines: Minerals, Energy and Chemical Engineering (WASM-MECE), Curtin University, Perth, WA 6845, Australia

Correspond Authors: meng.ni@polyu.edu.hk (M. Ni)

Facile Anion Engineering: A Pathway to Realizing Enhanced Triple Conductivity in Oxygen Electrodes for Reversible Protonic Ceramic Electrochemical Cells

Abstract

Reversible proton ceramic electrochemical cells (R-PCECs) have emerged as promising solutions for sustainable energy conversion and storage that can be operated at intermediate temperatures. However, the sluggish oxygen reduction reaction (ORR) and oxygen evolution reaction (OER) kinetics at the air electrodes of R-PCECs limit the cell performance. To achieve improved ORR/OER catalytic performance, we propose a practical approach of strategic anion engineering on the oxygen site of air electrode materials. Specifically, the popular triple $H^+/e^-/O^{2-}$ conducting oxide (TCO) $Ba_{0.5}Sr_{0.5}Co_{0.8}Fe_{0.2}O_{3-\delta}$ (BSCF) is selected to enhance the limiting H^+/O^{2-} generation and migration processes as an efficient air electrode for R-PCECs. By introducing different electronegative elements (F and Cl) to weaken metal-oxygen bonds (M-O), the oxygen chemical environment of the electrode material was optimized, thereby promoting surface oxygen exchange and O^{2-}/H^+ bulk migration. The resulting $Ba_{0.5}Sr_{0.5}Co_{0.8}Fe_{0.2}O_{2.9-\sigma}F_{0.1}$ electrode exhibits enhanced proton uptake/mobility and catalytic activity for ORR and OER as well as improved stability. This research offers a rational design strategy for engineering high-performance R-PCEC air electrodes with enhanced operating stability for efficient and sustainable energy conversion and storage.

Keywords: reversible protonic ceramic electrochemical cells (R-PCEC); Triple $H^+/e^-/O^{2-}$ conducting oxide (TCO); Metal-oxygen bonds (M-O); Oxygen reduction reaction (ORR); Oxygen evolution reaction (OER).

1. Introduction

The reversible solid oxide cells (R-SOCs) are promising for efficient energy conversion and storage [1-3], which can directly oxidize various fuels (hydrogen, hydrocarbons, ammonia, etc.) to produce electricity in fuel cell (FC) mode and store excess energy from renewable sources in electrolysis (EC) mode [4-6]. Operating at approximately 800°C, R-SOCs exhibit cost-effectiveness, environmental friendliness, and high efficiency, rendering them well-suited for large-scale energy conversion and storage applications [7, 8]. However, the notably elevated operational temperature of them gives rise to significant drawbacks, such as increased system costs, intricate thermal management requirements, sluggish startup, and diminished durability[9]. In contrast, the reversible protonic ceramic electrochemical cells (R-PCECs) utilizing proton-conducting electrolytes demonstrate a lower temperature range of approximately 400-700°C. These R-PCECs exhibit several advantages over R-SOCs, encompassing a reduced activation energy for proton transport (higher ionic conductivity), decreased working temperature (promoting swift startup and enhanced durability), elevated fuel utilization, and diminished cost. Consequently, R-PCECs emerge as promising candidates for energy conversion and storage (as illustrated in Fig. 1) [10-12].

Up to now, one technical challenge faced by high-performance R-PCEC is the notoriously sluggish oxygen reduction reaction (ORR) and oxygen evolution reaction (OER) at the air electrodes at reduced temperatures [9, 13, 14]. Actually, in R-PCEC, the ORR involves several sub-steps, such as surface oxygen adsorption and dissociation, reduction of oxygen molecules or atoms to different ionized oxygen species, bulk diffusion, combination of oxygen species and transported protons to form water, and H_2O desorption (fuel cell mode in Fig. 1) [13, 15].

Similarly, the OER involves adsorption/dissociation of water molecules, proton formation, proton transport to the electrolyte, and oxygen product formation and desorption (electrolysis mode in Fig. 1) [16, 17]. Hence, a perovskite oxide with excellent triple conductivity for $H^+/e^-/O^{2-}$ (triple conducting oxide, TCO) would be an ideal bifunctional air electrode for R-PCEC due to the significantly enlarged active reaction sites and greatly improved reaction kinetics. Accordingly, extensive efforts have been devoted by researchers to find effective methods to develop oxygen electrodes with high triple conduction properties. One commonly employed approach is to prepare composite electrodes by mechanically mixing ionic/electronic conductors with proton-conducting phases, such as $La_{0.6}Sr_{0.4}Co_{0.2}Fe_{0.8}O_{3-\delta}$-$BaZr_{0.5}Pr_{0.3}Y_{0.2}O_{3-\delta}$ (LSCF-BZPY)[18], $Sm_{0.5}Sr_{0.5}CoO_{3-\delta}$- $Ba(Zr_{0.1}Ce_{0.7}Y_{0.2})O_{3-\delta}$ (SSC-BZCY)[19] and $La_{0.6}Sr_{0.4}Co_{0.2}Fe_{0.8}O_{3-\delta}$-$BaCe_{0.5}Zr_{0.35}Y_{0.15}O_{3-\delta}$ (LSCF-BZCY)[20], etc. Unfortunately, the practical use of composite electrodes can be hindered by issues such as delamination caused by a mismatch in thermal expansion coefficient (TEC) of each phase and poor stability due to high steam concentration[13]. Another approach is to modify the surface properties [21, 22], such as infiltrating BCFZY into porous air electrode skeleton ($BaCe_{0.6}Zr_{0.3}Y_{0.1}O_{3-\delta}$)[23], which demonstrated a good electrochemical performance. However, the infiltration maybe unpredictable and time-consuming. In contrast, doping rare earth metals and transition metals into the proton conducting electrolytes ($BaZrO_3$/$BaCeO_3$) to create materials such as $BaCe_{0.5}Bi_{0.5}O_{3-\delta}$(BCBi), cobalt-substituted $BaZr_{0.1}Ce_{0.7}Y_{0.2}O_{3-\delta}$ and $BaZrO_3$, $BaCo_{0.4}Fe_{0.4}Zr_{0.1}Y_{0.1}$(BCFZY) has proven to be an effective strategy for air electrode development. However, the air electrodes developed by this strategy may suffer from high TEC values and low proton conductivity[11, 24-28]. Therefore, it is imperative to develop a

monolithic material with high triple $H^+/e^-/O^{2-}$ conductivity characteristics.

The state-of-art $Ba_{0.5}Sr_{0.5}Co_{0.8}Fe_{0.2}O_{3-\delta}$ (BSCF), as reported as a typic TCO, shows excellent performance as an air electrode for SOFC but its performance for PCFC is low, partly due to the low proton conductivity and sluggish ORR catalytic activity in a water-containing environment at intermediate temperatures[29, 30].Therefore, to further improve the electrocatalytic activity of the BSCF perovskite oxide, A-and B-site cationic doping involving the introduction of elements such as potassium (K), praseodymium (Pr), and phosphorus (P) into lattice of based oxides has been employed to derive $Ba_{0.4}K_{0.1}Sr_{0.5}Co_{0.8}Fe_{0.2}O_{3-\delta}$ (BKSCF), $PrBa_{0.5}Sr_{0.5}Co_{1.5}Fe_{0.5}O_{5+\delta}$ (PBSCF), and $Ba_{0.5}Sr_{0.5}(Co_{0.8}Fe_{0.2})_{0.95}P_{0.05}O_{3-\delta}$ (BSCFP0.05) functional air electrode materials with improved ORR/OER. [31-33]. Other peculiar cathode materials with triple conduction properties ($H^+/e^-/O^{2-}$) have been substantially improved for proton conducting oxides (PCO) applications by doping either Zr, Ni, or Mg in their lattice as in the case of $Sr_2Fe_{1.5}Mo_{0.5}O_{6-\delta}$[34], $La_{0.8}Sr_{0.2}CoO_{3-\delta}$ [35]and BCFZY[15, 36]. It should be emphasized that the enhanced ORR/OER catalytic performance of these doped electrodes mainly due to the increased oxygen vacancy concentration and improved proton uptake and conduction properties of the modified material. In fact, in addition to cationic site substitution, anionic (O) site doping has also been considered as an effective way to tune the diffusion behavior of the conducting species in oxides to achieve desired characteristic[37-39]. However, only few related works have been reported about the ORR/OER catalytic performance regulation of TCO air electrodes through anion engineering.

Herein, we propose a practical approach of systematically introducing a small amount of anion substitution on the oxygen site of a prominent cathode material, BSCF, to achieve a superior

TCO air electrode. Through the utilization of different electronegative elements ($F^{-}>O^{2-}>Cl^{-}$), the oxygen chemical environment within the material matrix was altered, leading to the weakening the metal-oxygen chemical bond and more high-efficiency O^{2-}/H^{+} transport paths. This modification promotes the surface oxygen exchange and bulk migration ability of the electrode, and significantly improves its proton uptake and conduction performance under aqueous conditions. The resulting electrode exhibits enhanced ORR/OER catalytic activity, offering a rational design strategy for engineering and improving high-performance R-PCEC triple conductivity air electrodes with favorable operating stability.

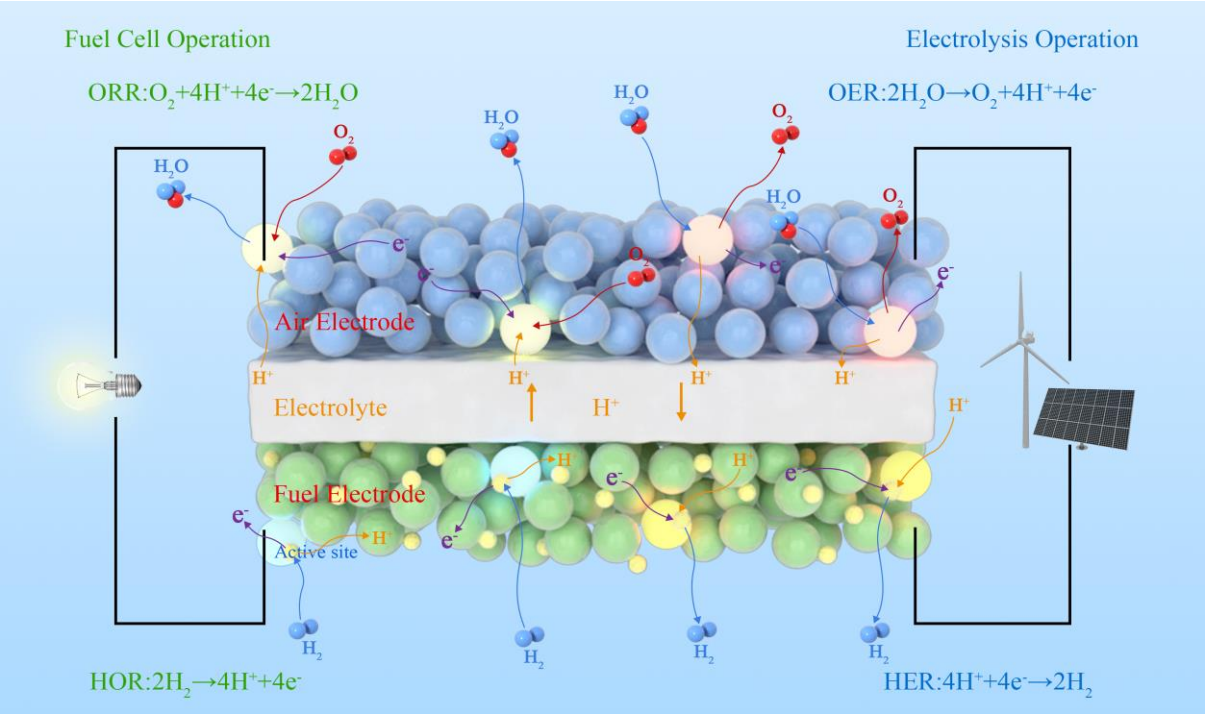

Fig. 1 Schematic diagram of R-PCEC in fuel cell and electrolysis operation modes

2. Results and discussion

As previously mentioned in the experimental section, the primary anion dopants (F^- and Cl^-) substituted into the oxygen sites of BSCF was achieved through the partial replacement of the traditional Sr $(NO_3)_2$ with SrF_2 or $SrCl_2$ compounds during the synthesis process. The remarkable stability of SrF_2 or $SrCl_2$, as shown in Fig. S1, confirms the possibility of successful incorporation of F^- and Cl^- into the lattice structure of the BSCF during high temperature sintering process. Fig. 2 (a-c) show the refined room temperature XRD patterns of BSCF and the fluorinated and chlorinated BSCF, $Ba_{0.5}Sr_{0.5}Co_{0.8}Fe_{0.2}O_{2.9-\sigma}F_{0.1}$ (BSCFF) and $Ba_{0.5}Sr_{0.5}Co_{0.8}Fe_{0.2}O_{2.9-\sigma}Cl_{0.1}$ (BSCFC) after calcination for 1000 ºC in ambient air. Fig. 2 (d) compares the unrefined diffraction patterns of the BSCFF, BSCFC, and BSCF. The diffraction peaks confirm that the anions (F^- and Cl^-) were successfully incorporated in the lattice structure of the BSCF without any impurity phase (such as SrF_2 or $SrCl_2$ secondary phases). The Rietveld refinement results indicated that BSCF, BSCFF and BSCFC perovskite oxide all have a cubic structure with a space group Pm-3m. From Fig. 2 (d), the higher diffraction angle of BSCFF from 30.7º to 32.5º indicate a contraction in its lattice size compared to BSCF while the shift of the diffraction pattern of BSCFC to a lower diffraction angle confirms an expansion in its lattice size[40]. This observed contraction and expansion in the lattice of BSCF could be attributed to the smaller ionic radius of F^- (1.33 Å) and larger ionic radius of Cl^- (1.81 Å) compared with O^{2-} (1.40 Å)[41, 42]. This observed phenomenon was also corroborated with the Rietveld refinements in Fig. 2 (a-c). The lattice parameters of BSCF are a = b = c = 3.986 Å while those of BSCFF and BSCFC were 3.977 Å and 3.995 Å, respectively. Considering the reliability factors R_p (unweighted) and R_{wp} (weighted profile factors R_p) are all around 10% of

these three oxides, the fitted results were very reliable, which illustrates a sound agreement between the observations in Fig. 2 (a-c) and Fig. 2 (d).

The HR-TEM images of BSCF, BSCFF and BSCFC samples (Fig. 2 (e-g)) present the arrangement of the crystalline fringes with the corresponding d-spacing (100 lattice plane distances) estimated to be 3.987 Å, 3.976 Å, 3.997 Å, respectively, which intimately agree with the Rietveld results and the shifted direction of the diffraction peaks. The Energy dispersive spectroscopy (EDS) mapping results in Fig. 2 (h-i) indicate that the anion elements (F and Cl) and the other elements (Ba, Sr, Co, Fe, O) were uniformly distributed in the lattice of BSCFF and BSCFC without any obvious segregation (Fig. S2). In addition, the mass percentage of the incorporated anion is close to the targeted value according to the Ion Chromatography result (Fig. S3), which further demonstrated the accuracy of the chemical formulas of perovskite oxide after high-temperature sintering. These results highly confirmed that the anion dopants F^- and Cl^- were well incorporated into the oxygen site of the oxide lattice as targeted through the ethylenediaminetetraacetic acid-citric acid (EDTA–CA) complexing sol-gel process for both BSCFF and BSCFC samples.

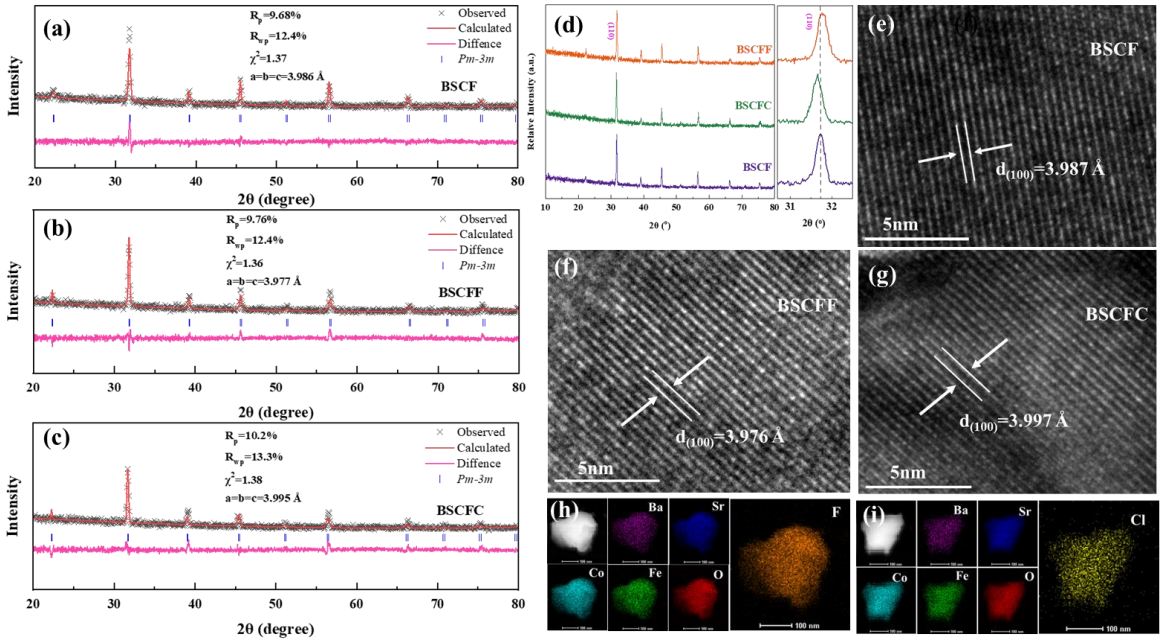

Fig. 2 The XRD Rietveld refinement profiles of (a) BSCF, (b) BSCFF and (c) BSCFC powders; (d) RT- XRD patterns of BSCF, BSCFF and BSCFC with a local enlargement; HR-TEM images of (e) BSCF, (f) BSCFF and (g) BSCFC samples; The elements distribution of (h) BSCFF and (i) BSCFC.

As the oxygen electrode functional material of R-PCEC, the high ORR/OER catalytic activity is closely related to the intrinsic oxygen environment in the lattice structure of oxygen electrodes. Hence, the concentration of oxygen vacancies plays an important role in achieving superb ORR catalytic performance. Iodometric titration and thermo-gravimetric analysis were carried out to determine the oxygen non-stoichiometry (δ) of all the investigated samples in room temperature and high temperature, respectively. The results depicted in Fig S4 reveal a gradual reduction in the δ value of the BSCF oxide samples, from 0.346 to 0.319, upon successful incorporation of F^- and Cl^-. This reduction indicates a decrease in the concentration of oxygen vacancies. Such an effect is attributable to the electron-neutral rule, wherein F^- and Cl^-, with less negative charge, replace the O^{2-} site. This replacement leads to a corresponding reduction in the number of oxygen vacancies exhibiting positive charge characteristics[42-44]. Additionally, anion dopants may also occupy the site of oxygen vacancies resulting in a

diminution, as shown in Equation (1) by Kröger–Vink notation[42, 44, 45]:

$$F^{-}\ (Cl^{-}) + V_O^{\cdot\cdot} \rightarrow F_O^{\cdot}\ (Cl_O^{\cdot}) \quad (1)$$

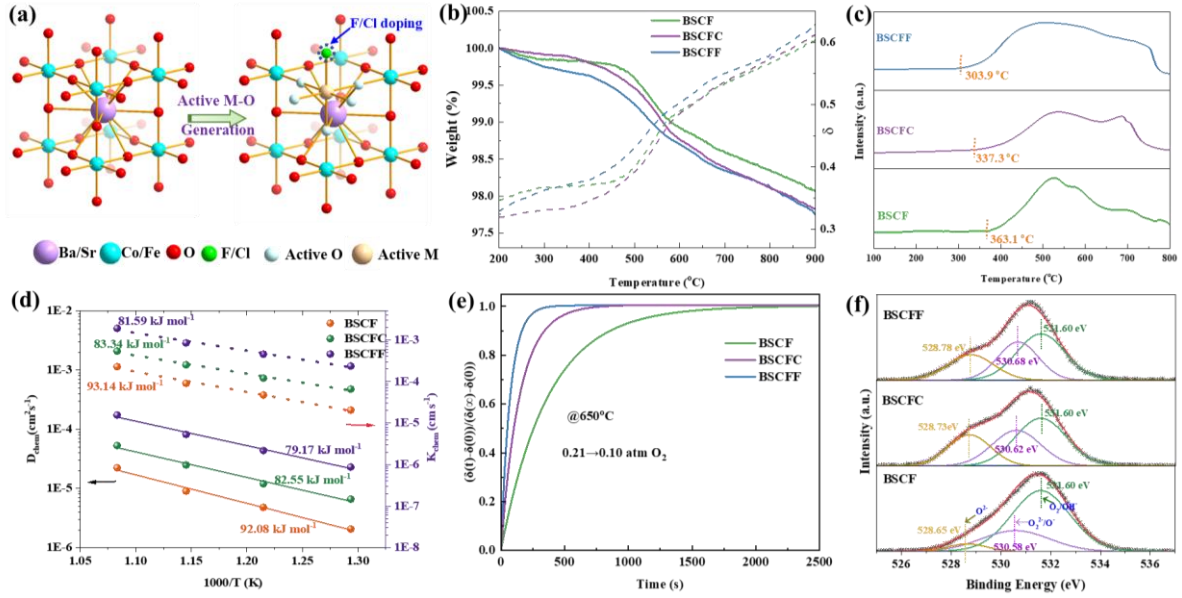

Fig. 3 (a) Schematic diagram of the process of substituted the O site of perovskite oxide with F/Cl and generate highly active metal-oxygen bonds (M-O); The different characterizations of BSCF, BSCFF and BSCFC samples: (b) recorded TGA profiles under dry air; (c) O_2-TPD curves in the temperature range of 100 to 800 °C; (d) the comparison of fitted D_{chem} and K_{chem} values at various elevated temperatures and the corresponding Arrhenius plots; (e) the fitting ECR response curves at 650 °C when sudden change the oxygen partial pressure from 0.21 atm to 0.1 atm; (f) the XPS spectra of O-1s.

Fig. 3 (a) exemplifies the mechanism of O site substitution in perovskite oxides with F/Cl in the lattice structure to achieve a highly active metal-oxygen bonds (M-O)[38]. The thermal gravimetric analysis (TGA) curves presented in Fig. 3 (b) demonstrate that the weight loss of BSCFF and BSCFC was greater than that of BSCF within the elevated temperature range of 200 °C to 900 °C (solid line). This indicates that approximately 10% more lattice oxygen is removed due to the anion doping, with an increase from 1.94% to 2.18% and 2.25% for Cl^{-} and F^{-} doping, respectively. Moreover, by combining iodometric titration and TGA analysis, the theoretically calculated oxygen non-stoichiometry of the three samples (dotted line, Fig. 3 (b)) revealed that BSCFF exhibited the highest oxygen vacancies value at high temperature,

although it was lower than that of the BSCF samples at room temperature. Similarly, BSCFC displayed a similar trend, indicating that the lattice oxygen in BSCFF/BSCFC was highly active at high temperature, which is beneficial for oxygen absorption and O^{2-} generation and transport processes, leading to enhanced ORR catalytic activity[46]. This is further supported by the O_2-TPD profiles of the three samples presented in Fig. 3 (c), wherein the initial desorption temperature of BSCF is decreased from 363.1 ºC to 337.3 ºC for BSCFC and 303.9 ºC for BSCFF. The lower temperatures of oxygen desorption are usually attributed to the valence change from tetravalent (Co^{4+}) to trivalent (Co^{3+})[47], suggesting that the reduction of B-site transition metal ions was promoted, and oxygen vacancy generation was much easier. These results preliminarily indicate that the metal-oxygen bond was in a more activated state after anion doping, which contributed to the acceleration of the ORR/OER of R-PCECs air electrodes.

The oxygen incorporation kinetics were evaluated using ECR measurements, by normalizing conductivity relaxation curves at different temperatures when the oxygen partial pressure was suddenly changed from 0.21 atm to 0.1 atm (Fig S5 (a-c)). These ECR response profiles provided important indicators associated with the chemical surface oxygen exchange and diffusion characteristics for BSCF, BSCFF, and BSCFC samples. Specific D_{chem} and K_{chem} values were fitted (Fig. 3 (d)) to investigate the effect of F^-/Cl^- incorporation. As shown in Fig. S5, the relaxation times of all samples gradually decreased with increasing temperature. However, after the successful incorporation of F/Cl in the O site of BSCF, the relaxation time was significantly reduced, as seen in Fig. 3 (e). For instance, the relaxation time is decreased from 1911 s for BSCF to 341 s for BSCFF and 706 s for BSCFC. This dramatic decrease

indicated the acceleration of the surface exchange and bulk transport process of oxygen after doping[36, 48]. Furthermore, the higher value of D_{chem} and K_{chem} for BSCFF and BSCFC than that of BSCF confirmed this result. The specific D_{chem} and K_{chem} values for BSCF were found to be 2.24×10^{-5} cm^2 s^{-1} and 2.28×10^{-4} cm s^{-1} at 650 ºC, respectively, which were close to the literature values[45]. The corresponding values for BSCFC and BSCFF were found to be significantly improved, at 5.31×10^{-5} cm^2 s^{-1} and 5.40×10^{-4} cm s^{-1} (more than doubled) for Cl doping, and 17.4×10^{-5} cm^2 s^{-1} and 19.1×10^{-4} cm s^{-1} for F doping (Fig. 3 (d) and Table S3). Additionally, the lower activation energy value for BSCFF (79.17 kJ mol^{-1}, 81.59 kJ mol^{-1}) and BSCFC (82.55 kJ mol^{-1}, 83.34 kJ mol^{-1}) compared with BSCF (92.08 kJ mol^{-1}, 93.14 kJ mol^{-1}) confirmed that the generation and surface transport of O-ions were prompted after doping. The faster surface exchange and bulk diffusion steps of oxygen are beneficial for the typical ORR/OER processes[15, 33].

In general, the results (more oxygen vacancies generated at high temperature, lower desorption temperature and significantly improved D_{chem} and K_{chem} values) indicated that the oxygen involved activities, such as the oxygen surface exchange and bulk oxygen transport processes, were significantly accelerated after doping on the O-sites of BSCF, thus exhibiting enhanced ORR/OER catalytic performance. These changes were most likely resulted from the altered O chemical environment and/or metal ions coordinated with it in the sample due to the dopant substitution at the O site of the perovskite[37, 43, 45, 49]. To gain further insights into the variability, XPS characterization was performed on the samples. As seen in Fig. 3 (f), the binding energy of the lattice oxygen (O^{2-}) were 528.65 eV, 528.73 eV and 528.78 eV for BSCF. BSCFC and BSCFF, respectively. This increase could be attributed to the fact that F^- or Cl^-

inclusion reduce the valence electron density of O^{2-}, weakening the chemical bonds between A- or B-site metal cations and oxygen ions, and making the lattice oxygen more active, which kept in line with the TGA and O_2-TPD results in this work and other reported results[49, 50]. Moreover, the chemical states and concentration of oxygen and B-site transition metals in these three samples have also undergone corresponding changes, as shown in Table S2 and Fig. S6, further indicating the presence of distinct chemical environments within the changed samples. For instance, electronic structure information of Co/Fe ions (B-site) indicated that the binding energy value of Co ions (both Co^{4+}/ Fe^{4+} and Co^{3+}/ Fe^{3+}) for BSCF was lower than that for BSCFC and BSCFF, which further demonstrated that the Coulombic force between B site metal cations and oxygen anions were weakened, and consequently, oxygen migration inside the bulk oxide as well as the oxygen transfer kinetics in the oxide surface would be accelerated[43, 45, 49]. This explains, at least in part, the improvement of D_{chem} and K_{chem} values of the F/Cl doped BSCF cathodes. Notably, F-doping had a more obvious lifting effect compared with Cl-doping due to the difference in electronegativity property between anionic dopants and oxygen[39]. The incorporation of F (χ=3.98) has higher electronegativity than oxygen (χ=3.44), while the other Cl (χ=3.16) is less electronegative, leading to a stronger ability of F^- to attract bonding electrons and increase the polarity of the metal-oxygen chemical bonds[41, 50]. This can be verified by the lowest binding energy of Co and the peak binding energy of oxygen for BSCFF. Therefore, the BSCFF air electrode exhibits a more active oxygen chemical environment with more efficient oxygen transport path and increased oxygen migration rate[39, 43]. And it can be seen more intuitively in Fig. 3 (a) which is a schematic diagram of the change (activation) mechanism of the oxygen chemical environment after anion-doping.

Excellent proton uptake and conduction capabilities are critical for oxide-based R-PCECs oxygen electrode materials to attain favorable ORR/OER catalytic performance. Currently, two possible mechanisms have been proposed for proton uptake, as shown in Equations (2, 3) [51, 52], where $V_O^{\cdot\cdot}$, $O_O^{\times}$ and $OH_O^{\cdot}$ represent oxygen vacancy, lattice oxygen and hydroxide ion occupying oxygen sites, respectively. It is evident from these equations that oxygen vacancies and lattice oxygen in the crystal structure of cathode materials play an essential role in proton uptake in the form of hydration or hydrogeneration.

Hydration mechanism: $O_O^{\times} + V_O^{\cdot\cdot} + H_2O \rightarrow 2\ OH_O^{\cdot}$ (2)

Hydrogenation mechanisms: $2\ O_O^{\times} + 2\ h^{\cdot} + H_2O \rightarrow 2\ OH_O^{\cdot} + 1/2\ O_2$ (3)

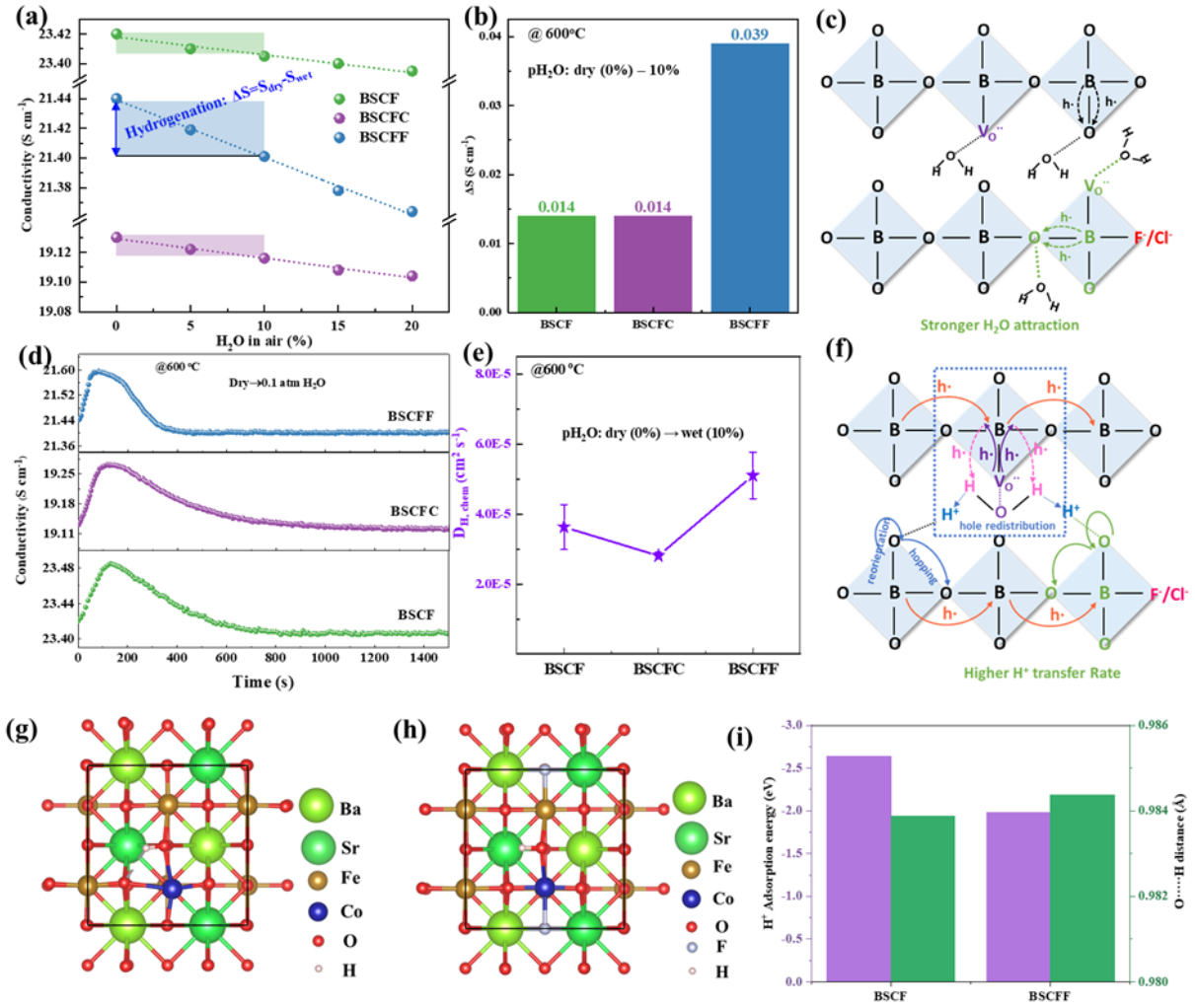

Fig. 4 Proton generation and mobility for BSCF, BSCFC and BSCFF samples: (a) the different

conductivity of bar samples at various H_2O partial pressure at 600 ºC; (b) the delta conductivity values (pH_2O: dry→10%) for three samples; (d) the typical ECR respond profiles when switching the atmospheres form dry air to air with pH_2O=0.1 atm at 600 ºC and (e) the comparison of fitted $D_{H,\,chem}$ values shown in Fig. 4 (d); schematic diagrams of (c) strong H_2O attraction and (f) higher H^+ migration properties of designed samples; Schematic illustration of H+ on Fe-O-Co in (g) parent BSCF and (h) BSCFF cell; (i) the O···H formation energy and distance comparison for BSCF(F) samples.

For the P-type conductor of BSCF based oxygen electrodes, which contains abundant oxygen vacancies and electron holes ($h^{\cdot}$), the intervention of protons is mainly through two forms of hydration reaction (Eq. (2)) and hydrogenation reaction (Eq. (3)), and as reported before[51], it appears that the hydrogenation reaction is the main mechanism of proton uptake in p-type oxygen electrodes. According to this mechanism, the proton incorporation process is spontaneous when the oxide material contains an abundance of holes, which act as sources to facilitate the conduction during the process, which can be confirmed by theories and previous research results[33, 34, 51, 53]. However, it should be noted that this reaction generates proton defects ($OH_O^{\cdot}$) at the cost of electron holes, which can result in a significant decrease in conductivity. Therefore, changes in electrical conductivity can reflect the hydrogenation reactivity of the sample in a humid atmosphere. To investigate the proton uptake properties of different cathodes, the conductivity of three bar samples (BSCF, BSCFC, and BSCFF) was tested at various H_2O partial pressures in air at 600 ºC (Fig. 4 (a)). The results showed that the electrical conductivity of all samples decreased significantly with increasing water partial pressure in the atmosphere, providing further evidence that proton absorption in BSCF-based cathodes is carried out may through the hydrogenation reaction. Furthermore, it can be tentatively concluded that the decrease in conductivity values for the three samples suggests that, compared with the BSCF and BSCFC test samples, the conductivity reduction of BSCFF is more pronounced. To better illustrate this change, the difference in conductivity between dry air and air containing 10% water (ΔS) was selected for comparison (Fig. 4 (b)). It is evident that the ΔS value of BSCF and BSCFC is 0.014 S cm^{-1}, while that of BSCFF increases significantly to 0.039 S cm^{-1} under the same conditions, indicating that BSCFF has a strikingly improved proton absorption capacity, producing more proton defects. This may be due to the introduction of strong electron affinity of fluorine that enhances the basicity of the anions in the perovskite lattice, and this active oxygen chemical environment is favorable for the

adsorption of water in the surrounding environment, thus showing enhanced hydrogenation (Fig. 4 (c))[49, 54]. In addition, as shown in Fig. 4 (c), the hydrogenation reaction may happen in the humid atmosphere accompanied by hydration reaction which consumed the oxygen vacancies to attach H_2O and produced proton defects accordingly. As mentioned earlier, the higher concentration of $V_O^{\cdot\cdot}$, which are the H_2O absorption sites of hydration, always have lower hydration energy, indicating that it is more favorable for the formation of protonic defects in fluorinated perovskites. It is worth emphasizing that the stronger H_2O attraction ability facilitate the progress of R-PCEC oxygen electrode ORR/OER rate.

Beyond the stronger proton uptake ability, the fast proton mobility is another particularly vital indictor for the choice of oxygen electrodes. Currently, there are two main theoretical proton conduction models for ORR processes in oxides: the vehicle mechanism and the Grotthuss mechanism[52]. According to the vehicle mechanism, protonic defects migrate via the diffusion of O^{2-}. In contrast, the Grotthuss mechanism proposes that protons hop from one O^{2-} to another by forming and breaking OH^- groups alternately after the first reorientation step-the OH^- group bends towards neighboring O^{2-} ions. Among the two mechanisms, the Grotthuss mechanism is widely accepted in protonic conducting oxides since the activation energy (Ea) of H^+ hopping in OH^- groups is much lower (<0.4 eV) than the low mobility of O^{2-}[52].

Considering that the proton conductivity in the cathode material is several orders of magnitude lower than the electron conductivity, it is difficult to accurately separate the proton conductivity from the total conductivity. Herein, a prudent ECR repones method through uplifting the H_2O partial pressure in testing atmosphere was applied to determine the values of chemical diffusion coefficient ($D_{H,chem}$) of proton to assess the migration of the protons (Fig. 4 (d))[55]. This is a feasible way to unravel the bulk diffusion of H^+ in air electrodes by solving the Fick diffusion equations based on the mechanism that all carries (oxygen vacancies, holes, and proton defects)

will be redistributed when introduce more water in operational environment. As shown in Fig. 4 (d), when the water partial pressure is switched from 0 atm to 0.1 atm at 600 °C, the electrical conductance of the BSCF sample first experienced a short period of rising, and then subsequently decreased until reaching a steady state, similar curve trends were also observed for BSCFF and BSCFC samples. These interesting non-monotonic relaxation curves can be explained by the phenomenon that the holes would redistribute accompanied by the proton transfer step (Fig. 4 (f))[54, 55]. During hydration or hydrogeneration process, the active O incorporation and bulk diffusion processes would generate holes, as shown in Equation (4), while the H is converted to H^+ by consuming a hole shown in Equation (5). This means that the active oxygen transport process in the sample would produce more electron holes and lead to an increase in conductivity, while the active hydrogen transport process would consume electron defects and lead to a decrease in conductivity. During the ECR response process, oxygen bulk diffusion and proton transport processes took place simultaneously, these two opposite effects on hole concentration led to a non-monotonic variation in the conductivity when the atmosphere is suddenly shifted, and similar results are also observed in the BCFZY, $Ba_{0.5}Sr_{0.5}(Co_{0.8}Fe_{0.2})_{0.95}P_{0.05}O_{3-\delta}$ (BSCFP0.05) and $Sr_2Fe_{1.5}Mo_{0.4}Zr_{0.1}O_{6-\delta}$ air electrodes[33, 34, 55].

$$O^* + V_O^{\cdot\cdot} \rightarrow O_O^{\times} + 2\,h^{\cdot} \quad (4)$$

$$OH^* + h^{\cdot} \rightarrow H^+ + O_O^{\times} \quad (5)$$

Based on various ECR profiles showing conductivity variation as a function of elapsed time with increasing pH_2O, different parameters of $D_{H,chem}$ were determined and summarized in Fig. 4 (e). It can be clearly observed that BSCFF sample exhibited the highest $D_{H,chem}$ value, which

was 5.11×10^{-5} cm^2 s^{-1}, while that of BSCF sample was only 3.64×10^{-5} cm^2 s^{-1} under the same conditions, and it was even a little lower for the BSCFC sample. Such a noticeable improvement of $D_{H,chem}$ manifested that the fluorinating BSCF perovskite oxide was an efficient way to enable more rapid proton bulk diffusion process in oxygen electrode material. This may be explained from several conveniences: Initially, owing to the increased electronegativity of fluorine, it manifests a heightened affinity for bonding electrons, resulting in a notable reduction in the electronic density surrounding adjacent oxygen atoms, thereby weakening the O···H interaction. Furthermore, as illustrated in Fig. 4(g-i), the BSCFF sample exhibits a higher positive formation energy for O···H chemical bonds when compared to the BSCF sample, as determined through DFT calculations. This discrepancy implies that protons form a more robust attachment to oxygen in the BSCF configuration compared to BSCFF, resulting in a hard hopping process based on the Grotthus mechanism. Additionally, extended O···H distances were also observed in fluorinated oxides, further underscoring the propensity for the disruption of O···H bonds. In essence, the fluorinated system would require a lower energy barrier for the displacement of protons from M-OH to an adjacent position [56]. Secondly, the introduction of F element causes a certain degree of lattice contraction, which shortens the O-O bonds distance along the intra-octahedron direction correspondingly. As previously noted, the O-O bond distance is exactly the proton hopping gap from one oxygen site to another neighboring oxygen ion site. Thus, the decreased hopping distance, meaning lower energy consumption, can accelerate the proton conduction, as the activation energy of proton transport is related not only to the proton reorientation energy but also to the proton hopping energy. From this point of view, the introduction of Cl element is unfavorable to proton

hopping process. Finally, the activation energy for proton conduction typically decreases with higher radius of B-site elements since the larger acceptor helps in tilting the octahedra[52]. And the B-site metal ions in BSCFF have significantly more Co^{3+} (0.61 Å) ions with larger radii than Co^{4+} (0.53 Å), which is also beneficial to the proton transport process. Combined with these factors which indexed a lower energy barrier and higher proton transfer property, it is foreseeable that the fluorinated BSCF shows greatly improved proton chemical diffusion coefficient.

The electrocatalytic performance of three electrodes were assessed in the BZCYYb proton-conducting electrolyte supported symmetrical cells with BSCF, BSCFC and BSCFF air electrodes between 450 °C and 650 °C. Electrochemical impedance spectroscopy (EIS) was used to compare the typical Nyquist plots in humid air at 600°C, as shown in Fig. 5 (a). The BSCFF electrode showed the lowest ASR value of only 0.12 Ω cm^2, whereas those of BSCF and BSCFC were 0.41 Ω cm^2 and 0.23 Ω cm^2, respectively. This indicates that the BSCFF air electrode has the best ORR catalytic performance.

To gain further insight into this noticeable improvement, the distribution of relaxation time (DRT) technology was applied by deconvoluting the corresponding EIS data to discriminate against a train of overlapping electrode processes (Fig. 5 (b)). Four characteristic peaks were observed in the DRT plots, denoted as three different segments according to the located frequency range: low frequency P1 (LF, <10 Hz), intermediate frequency P2 and P3 (IF, 10-10^3 Hz), and high frequency P4 (HF, >10^3 Hz). Specifically, referring to previously reported DRT analysis results and their corresponding peak patterns related to R-PCEC air electrode[33, 57, 58], as well as the actual ORR and OER processes involved shown in Fig. 6i, these can be

assigned to the electrochemical processes of gas (O_2/steam) diffusion (P1), surface exchange and/or ions (H^+/O^{2-}) transfer at the electrode bulk (P2 & P3), and ions/charge transfer from the electrolyte to the electrode at the triple-phase boundaries (P4) [59, 60]. Fig. 5 (b) showed that all characteristic peak areas for BSCFF (Cl) reduced compared to the pristine BSCF electrode, indicating that almost all interconnected sub-processes were accelerated during the cathode electrochemical reaction. Therefore, it exhibited a lower resistance for the whole oxygen reduction reaction.

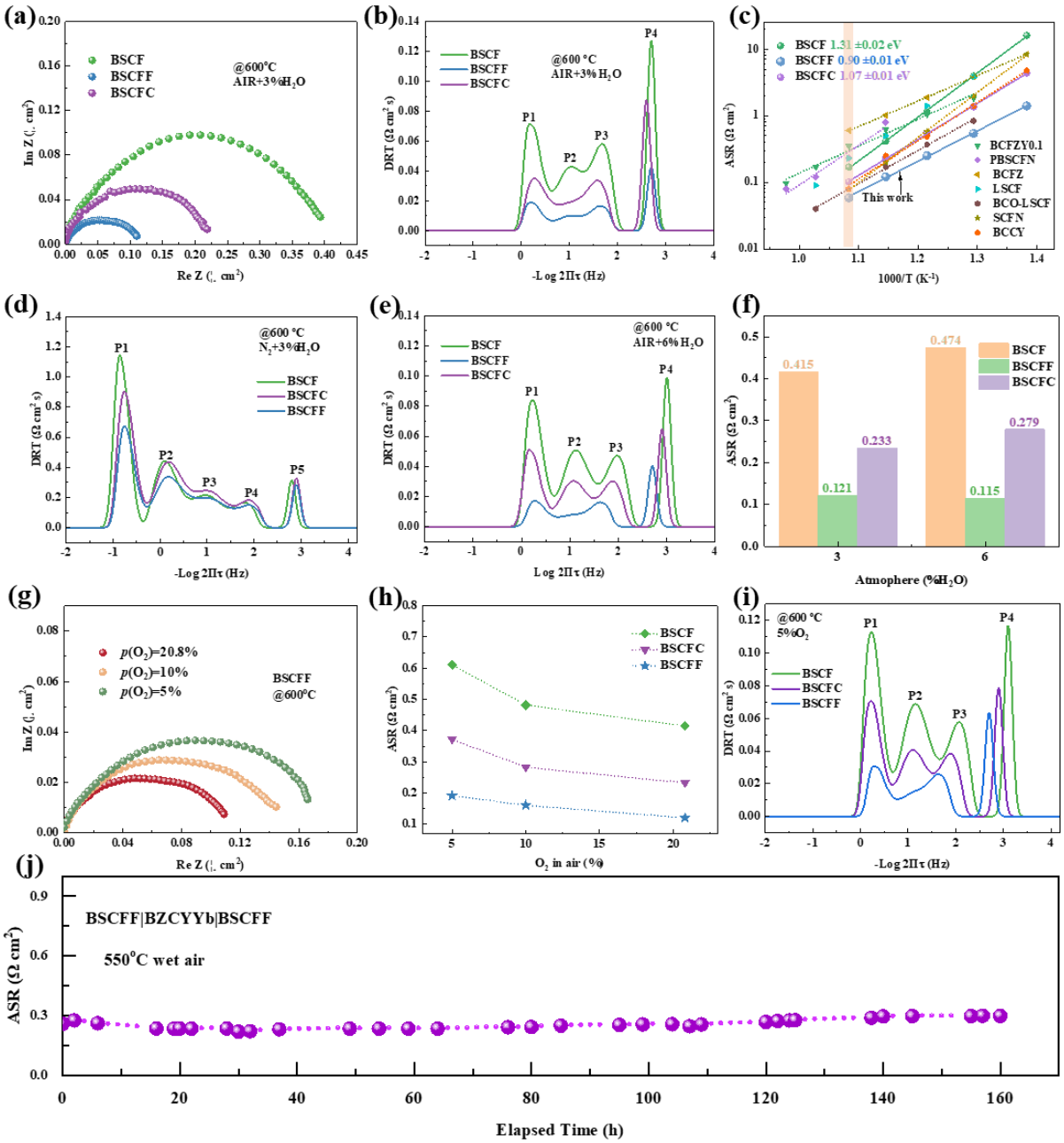

Fig. 5 The electrocatalytic activity of three samples: (a) the typical Nyquist plots of symmetrical cells at 600 °C in wet air; (b) the corresponding DRT analysis shown in ; (c) Arrhenius plots of ASR values as a function of temperatures in wet air; the DRT results in (d) wet N_2 and (e) 6%H_2O + air atmospheres; (f) the summarized ASR values at different H_2O partial pressure in air; (g) the Nyquist plots of BSCFF in different oxygen partial pressure; (h) the summarized ASR values variation with various O_2 content; (i) the DRT results in 5%O_2+95%N_2; (j) the long-term stability of symmetrical cell with the BSCFF electrodes.

In addition, the Arrhenius plots of the ASR values as a function of temperatures were summarized and used to compared with other high-performance cathodes based on BZCYYb electrolyte supported symmetrical cells in wet air, such as $BaCo_{0.4}Fe_{0.4}Zr_{0.1}Y_{0.1}O_{3-\delta}$ (BCFZY) ,

$PrBaCo_{1.6}Fe_{0.2}Nb_{0.2}O_{5+\delta}$ (PBCFN), $BaCo_{0.4}Fe_{0.4}Zr_{0.2}O_{3-\delta}$ (BCFZ), $La_{0.6}Sr_{0.4}Co_{0.2}Fe_{0.8}O_{3-\delta}$ (LSCF), barium cobaltite (BCO) coated LSCF, $Sr_{0.9}Ce_{0.1}Fe_{0.8}Ni_{0.2}O_{3-\delta}$ (SCFN), and self-assembled $BaCo_{0.7}(Ce_{0.8}Y_{0.2})_{0.3}O_{3-\delta}$ (BCCY) (Fig. 5 (c), Fig. S8 and Table S4). The BSCFF cathode still exhibited the smallest ASR value, and its electrode reaction activation energy (Ea) was also significantly reduced in comparison with other cathodes, at only 0.90 eV. Therefore, it may be more conducive to the low-temperature operation. These results preliminarily confirmed that a small amount of anion doping in BSCF perovskite was an effective way to improve the catalytic performance of R-PCEC oxygen electrode, and the introduction of F had a more significant effect on improving the electrode performance than Cl due to the higher-level enhanced oxygen and proton involved electrochemical reaction processes.

To further analyze the proton uptake and transport capabilities of the three electrodes in a humid atmosphere, the ASRs (Fig. S9) and DRT (Fig. 5 (d)) plots were carried out in humid nitrogen, eliminating the influence of O^2 diffusion, oxygen-related surface exchange, and O^{2-} transfer processes[24]. The DRT analysis results showed that the enhancement of fluorinated BSCF can be attributed to faster H_2O diffusion (P1) and proton transfer (P2-P4) sub-steps, which are consist with the stronger water attraction and protons transfer ability mentioned in Fig. 4. Moreover, when the water partial pressure is increased to 6% H_2O in air, the resistances of these samples (Fig. 5 (f)) showed a different trend. Both the impedance BSCFC and BSCF grew with amplitudes of 0.046 Ω cm^2 and 0.059 Ω cm^2, respectively, while that of BSCFF decreased from 0.121 Ω cm^2 to 0.115 Ω cm^2, which might be due to the different proton conductivity of these samples[61]. From the Nyquist plots (Fig. S10) and corresponding DRT analysis results (Fig. 5 (e)), it was because the remarkable accelerated water (g) diffusion and

consumption processes so that the ORR was progressively enhanced even in higher water content and lower oxygen levels[61]. This illustrated that outstanding formation and transfer of hydroxide defects of the BSCFF triple conducting oxide[62] are highly valuable for R-PCECs oxygen electrodes.

At the same time, to further investigate the influence of the oxygen concentration on the electrochemical reaction (ORR) kinetics of different electrode, we collected the EIS data (Fig. S12 and Fig. 5 (g)) of these symmetrical cells in the different oxygen partial pressure and performed the DRT analysis (Fig. 5 (i)). As expected, the electrode polarization impedance values for all electrodes increased abruptly with decreasing oxygen partial pressure. And according to the corresponding DRT diagram, the reduction of the oxygen partial pressure leads to a significant slowdown of each step reaction process, especially the low-frequency (P1) associated with gas (O_2) diffusion process and the intermediate-frequency (P2, P3) related to oxygen surface exchange activation and bulk phase transport process. However, as the comparison of ASR values (Fig. 5 (h)) for these samples and the corresponding DRT results shown, the fluorinated BSCF still exhibited the lowest resistance when the oxygen content reduced to only 5%, indicating that BSCFF electrode has the strongest ability to utilize oxygen to participate in the ORR, which is benefited from its abundant concentration of oxygen vacancies and weaker metal-O bonds[43, 62].

In addition, to gain more understanding of the electrochemical reaction kinetics of the BSCFF air electrode, the corresponding EIS curves and DRT plots under different water partial pressure (pH_2O) and oxygen partial pressure (pO_2) were applied to further demonstrate the elementary sub-step involved in the whole electrode reactions. As shown in Fig. S11 (a) and (b), the ASR

value was lower in higher pH_2O and pO_2, which further indicates the excellent proton and oxygen conduction ability of the BSCFF air electrode. As observed in Fig. S11 (c), the P4 (HF) and P3(IF) were significantly reduced with the increased pH_2O which prompts the formation and transfer of hydroxide defects[14], suggesting that the P4 and P3 might be strongly associated with the proton migration process from the electrolyte the electrode and the production of hydroxide defects at the electrode bulk. In the meantime, the P1 (LF) was sightly dropped with the increased pH_2O, suggesting the P1 correlated with the water(g) mass diffusion process. Moreover, the P2 shows a different change tendency, firstly declining and then increasing with the increased pH_2O. As the inlet water(g) maybe consume the concentration of oxygen vacancies generated in the electrode material, the higher content of steam in the testing atmosphere can lead to a detrimental effect on the oxygen transport process. Therefore, the P2 can be linked with the process of oxygen transport in the electrode bulk, which can be further illustrated by the results of the various pO_2 effect on the electrode reactions displayed in Fig S11 (d). It can be clearly seen that all peaks reduced with the higher pO_2, which keeps consistent with some previous reports[14, 33, 60], indicating that all peaks can relate to the oxygen-involved sub-steps of electrode reactions. Combined with the location of the peaks (characteristic frequency), the P1 (LF) may correspond to the oxygen gas diffusion process; the P2 (IF) was associated with the oxygen transfer in the electrode bulk while the P3(IF) likely linked with the production of the O^{2-}; the P4 (HF) may be related with charge transfer process involved in ORR processes. In conclusion, the electrochemical processes corresponding to the characteristic peaks observed in the DRT plots keep line with the mentioned analysis results (considering both the influence of pH_2O and pO_2).

The EIS and DRT results all imply that BSCFF has superior electrocatalytic activity, and the excellent catalytic performance can be operated in a long time, which can be confirmed by the long-term stability of the symmetrical cell in humid air at 550 ºC with a configuration of BSCFF|BZCYYb|BSCFF (Fig. 5 (j)). After 160 h of operation, the evaluated ASR values remained around 0.28 Ω cm^2 without any significant degradation, implying a remarkable stability of the BCSFF electrode on the BZCYYb proton-conducting electrolyte in water-containing atmosphere. This electrode with efficient and stable electrocatalytic activity is very suitable for use as an oxygen electrode based on proton conductor electrolyte cells.

To verify the superior ORR catalytic performance of the BSCFF oxygen electrode in fuel cell (FC) mode, the NiO-BZCYYb anode supported single cells with BSCF, BSCFC and BSCFF cathodes were fabricated and tested. The typic i-V-p curves comparison of these cells, supplying pure H_2 and air to anode and cathode sides at 650 ºC, are shown in Fig. 6 (a). It is evident that the cell with BSCFF oxygen electrode exhibited the highest peak power density (PPD) of 977 mW cm^{-2}, while the parent perovskite BSCF cathode the chlorine BSCF electrode achieved only 657 mW cm^{-2} and 770 mW cm^{-2}, respectively. Similar trends were observed in the detailed i-V-p curves recorded at 600-450 ºC (Fig. 6 (b) and Fig. S13), further confirming the superior ORR catalytic activity of the fluorine modified BSCF cathode. Remarkably, the PPDs of 668, 472, 303, 215 mW cm^{-2} were reached for BSCFF air electrode at 600, 550, 500 and 450 ºC, respectively, and the corresponding open circuit voltages (OCVs) all achieved above 1.05 V, indicating the electrolyte film is dense which further illustrated by the SEM images (Fig. S14). When compared to state-of-art oxygen electrodes reported so far, such as $PrNi_{0.5}Co_{0.5}O_{3-\sigma}$ (PNC), $BaCo_{0.7}(Ce_{0.8}Y_{0.2})_{0.3}O_{3-\delta}$ (BCCY), $Sr_{0.9}Ce_{0.1}Fe_{0.8}Ni_{0.2}O_{3-\delta}$ (SCFN),

$SrEu_2Fe_{1.8}Co_{0.2}O_{7-\delta}$ (SEFC), $Sr_3Fe_2O_{7-\sigma}$ (RP-SF), $(PrBa_{0.8}Ca_{0.2})_{0.95}Co_2O_{6-\delta}$ (PBCC95), $BaCe_{0.5}Fe_{0.3}Bi_{0.2}O_{3-\delta}$ (BCFBi), $BaCo_{0.4}Fe_{0.4}Zr_{0.1}Y_{0.1}O_{3-\sigma}$ (BCFZY), the electrochemical performance of the prepared PCFC based on the fluorine BSCF achieved a rarely high PPD in fuel cell mode (Fig. 6 (c) and Table S5). The impressive performance can be related to the enhanced oxygen and proton kinetic rate of transport and surface diffusion so that it showed accelerated ORR catalytic activity which could be further demonstrated by the significantly lower ASR value, that were only 0.08 and 0.19 Ω cm^2 under OCV condition at 650 and 600 °C, respectively (Fig. S15). To clearly highlight the operational stability of the BSCFF air electrode, the long-term durability test of this single cell under a constant current density of 0.38 A cm^{-2} at 550 °C was conducted (Fig. 6 (d)). It can be found that the cell voltage didn't show detectable degradation and stabilizes at around 0.78 V during the 60-h operation. At the same time, the inset SEM image also identified that the BSCFF air electrode had a good contact with the electrolyte film without any breaks after the test, which suggested that the BSCFF cathode and BZCYYb electrolyte film had a good thermal expansion coefficient matching and thermal stability in fuel cell mode.

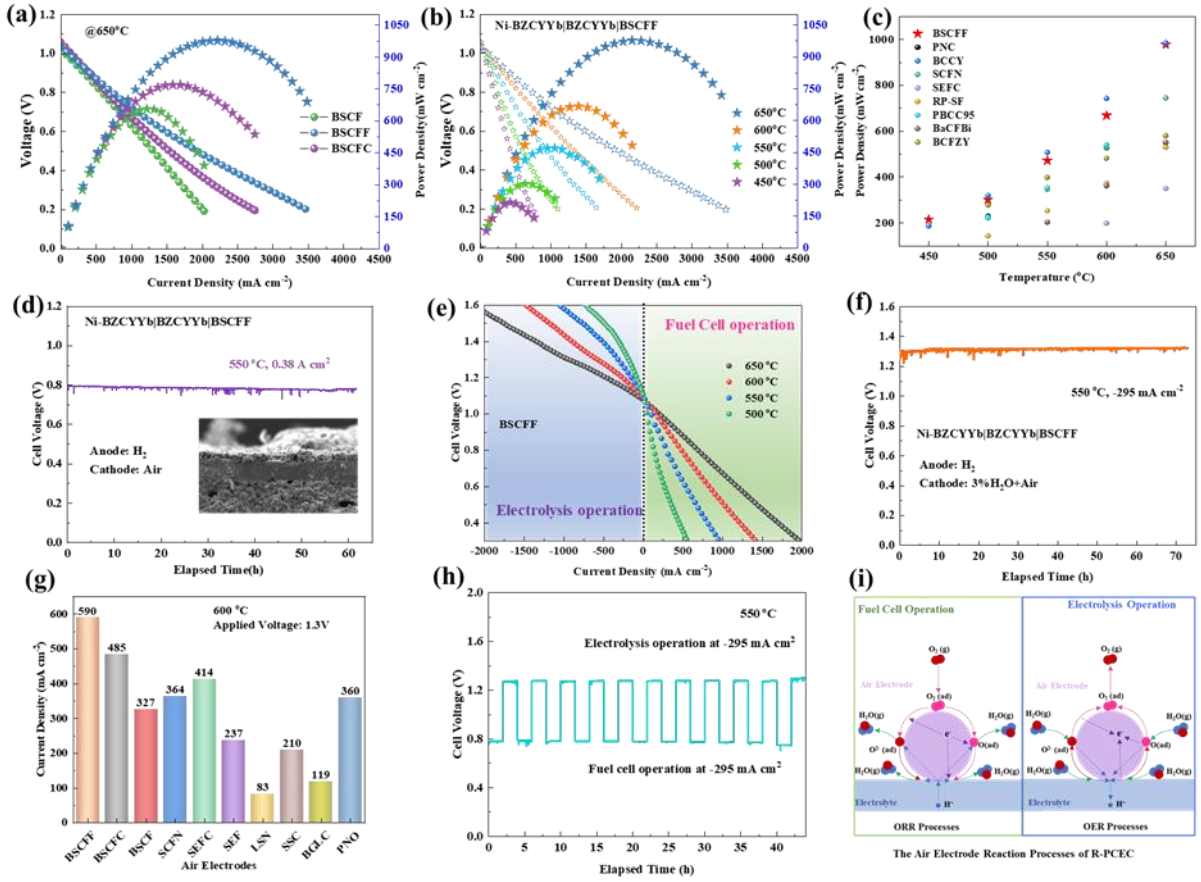

Fig. 6 (a) The comparison of i-V-p curves for NiO-BZCYYb supported cell with BSCF, BSCFC and BSCFF air electrodes at 650 °C; (b) the i-V-p curves of the cell with BSCFF oxygen electrode at 450-650 °C; (c) PPDs comparison of PCFCs with different cathodes, BSCFF (this work) and other cathodes,; (d) durability of the single cell with BSCFF cathode at 550 °C under a current density of 0.38 A cm^{-2}; (e) the i-V curves of R-PCEC with dry H2 and wet air (3% H_2O) as the reactant gas in both fuel cell and electrolysis operations at 500-650 °C with BSCFF oxygen electrode; (f) operating stability of R-PCEC at 550°C; (g) the current density comparison of R-PCEC at 1.3V with various air electrodes; (h) continuous R-PCEC operation, cycling between electrolysis and fuel cell mode at 550 °C; (i) schematic illustration of the ORR/OER processes for air electrodes operating at fuel cell and electrolysis mode.

Moreover, to confirm the excellent electrocatalytic activities of BSCFF air electrode in R-PCEC mode, similar single cells with different oxygen electrodes were also prepared for electrochemical reversibility measured. The i-V curves of R-PCEC with the parent BSCF air electrode and the corresponding fluorine and chlorine BSCF air electrodes were obtained by inletting the pure H_2 and 3% H_2O-air to fuel and air electrodes, respectively (see Fig. 6 (e) and Fig. S16). The assembled R-PCEC operated in fuel cell mode had lower power output than the

proton ceramic fuel cell due to the slight difference in cell preparation and the introduction of steam in the air electrode[24]. It can be clearly observed that when the reversible cells function in electrolysis cell (EC) mode and the applied voltage was 1.3V for BSCFF electrode, the electrolysis current density could achieve 950, 590, 316, 190 mA cm^{-2} at 650, 600, 550 and 500 °C. The electrolysis performance was higher than those of the BSCF and BSCFC oxygen electrodes and exceeded many reported state-of-art air electrode (Fig. 6 (g)) utilized in R-PCEC, such as $Sr_{0.9}Ce_{0.1}Fe_{0.8}Ni_{0.2}O_{3-\delta}$ (SCFN), $SrEu_2Fe_{1.8}Co_{0.2}O_{7-\delta}$ (SEFC), $SrEu_2Fe_2O_{7-\delta}$ (SEF), $La_{1.2}Sr_{0.8}NiO_4$ (LSN), $Sm_{0.5}Sr_{0.5}CoO_{3-\delta}$ (SSC), $BaGd_{0.8}La_{0.2}Co_2O_{6-\delta}$ (BGLC) , $Pr_2NiO_{4+\delta}$ (PNO) (Table S6). Furthermore, the electrolysis operational stability test for this cell in EC mode was carried out at 550 °C. It can be directly observed that the electrolysis performance of BSCFF kept stable without obvious degradation under a constant electrolysis current density of -295 mA cm^{-2}, which further demonstrated the superiority of BSCFF electrode.

To further confirm the feasibility of R-PCEC with this advanced BSCFF oxygen electrode, cell reversibility was also evaluated by cyclic switching between the electrolysis hydrogen production (-295 mA cm^{-2}) and power generation modes (295 mA cm^{-2}) under different current density conditions at 550 °C, and it has run stably throughout 11 reversible cycles within 44h (2h each condition) without negligible performance degradation (Fig. 6 (h)). The reliable conversion operation under different current densities strongly revealed that BSCFF air electrode has good durability and chemical stability, as well as excellent adhesion and compatibility with the electrolyte. These results suggest that BSCFF is a potential oxygen electrode material for R-PCEC (Fig. 6 (i)) with high activity and durability.

3. Conclusion

In summary, the more active oxygen chemical atmosphere was achieved by tuning the metal-oxygen bond of BSCF triple-conducting ($H^+/e^-/O^{2-}$) perovskite oxide via different electronegativity anions (F^-, Cl^-) doping. The chemical properties of these samples were systematically investigated, and all results revealed that an optimal F^--dopant with greater electronegativity enhanced the bulk oxygen/proton diffusion, surface oxygen exchange and proton uptake characteristics, and benefiting from these positive effects, significantly accelerated the sluggish ORR/OER kinetics of the parent BSCF air electrode, which ensuring the excellent electrochemical performance of the BSCFF catalyst in both fuel cell (FC) mode and electrolytic cell (EC) mode. The peak power density of single cell working in FC mode reached 977 mW cm^{-2} at 650 ºC, and the current density of the EC mode reached 950 mA cm^{-2} at applied voltage of 1.3V. The cycle operation of power generation and hydrogen production under different current densities was further demonstrated the high adaptability and durability of the BSCFF catalyst assembled as the R-PCEC air electrode. This approach, modulating the chemical bonding interactions based on anions-doping in perovskite cathodes, offers a rational design for functional material to improved electrochemical performance of energy storage and conversion devices based on proton conductors, and has guides significance for the exploration of catalysts in other electrochemical systems.

Acknowledgement

We thank the grants (Project Number: N_PolyU552/20) from Research Grants Council, University Grants Committee, Hong Kong SAR, and National Nature Science Foundation of China (22209138), Guangdong Basic and Applied Basic Research Foundation (2021A1515110464).

Reference

[1] R. Murphy, Y. Zhou, L. Zhang, L. Soule, W. Zhang, Y. Chen, M. Liu, A new family of proton-conducting electrolytes for reversible solid oxide cells: $BaHf_xCe_{0.8-x}Y_{0.1}Yb_{0.1}O_{3-\delta}$, Adv. Funct. Mater. 30(35) (2020) 2002265.https://doi.org/10.1002/adfm.202002265.

[2] S. Choi, T.C. Davenport, S.M. Haile, Protonic ceramic electrochemical cells for hydrogen production and electricity generation: exceptional reversibility, stability, and demonstrated faradaic efficiency, Energy Environ. Sci. 12(1) (2019) 206-215.https://doi.org/10.1039/C8EE02865F.

[3] E. Vøllestad, R. Strandbakke, M. Tarach, D. Catalán-Martínez, M.-L. Fontaine, D. Beeaff, D.R. Clark, J.M. Serra, T. Norby, Mixed proton and electron conducting double perovskite anodes for stable and efficient tubular proton ceramic electrolysers, Nat. Mater. 18(7) (2019) 752-759.https://doi.org/10.1038/s41563-019-0388-2.

[4] S.Y. Gómez, D. Hotza, Current developments in reversible solid oxide fuel cells, Renew. Sust. Energ. Rev. 61 (2016) 155-174.https://doi.org/10.1016/j.rser.2016.03.005.

[5] F.M. Sapountzi, J.M. Gracia, C.J. Weststrate, H.O.A. Fredriksson, J.W. Niemantsverdriet, Electrocatalysts for the generation of hydrogen, oxygen and synthesis gas, Prog. Energy Combust. Sci. 58 (2017) 1-35.https://doi.org/10.1016/j.pecs.2016.09.001.

[6] B. Hua, N. Yan, M. Li, Y.-F. Sun, Y.-Q. Zhang, J. Li, T. Etsell, P. Sarkar, J.-L. Luo, Anode-Engineered protonic ceramic fuel cell with excellent performance and fuel compatibility, Adv. Mater. 28(40) (2016) 8922-8926.https://doi.org/10.1002/adma.201602103.

[7] C. Graves, S.D. Ebbesen, S.H. Jensen, S.B. Simonsen, M.B. Mogensen, Eliminating degradation in solid oxide electrochemical cells by reversible operation, Nat. Mater. 14(2) (2015) 239-244.https://doi.org/10.1038/nmat4165.

[8] M.B. Mogensen, M. Chen, H.L. Frandsen, C. Graves, J.B. Hansen, K.V. Hansen, A. Hauch, T. Jacobsen, S.H. Jensen, T.L. Skafte, X. Sun, Reversible solid-oxide cells for clean and sustainable energy, Clean Energy 3(3) (2019) 175-201.https://doi.org/10.1093/ce/zkz023.

[9] Y. Zhou, E. Liu, Y. Chen, Y. Liu, L. Zhang, W. Zhang, Z. Luo, N. Kane, B. Zhao, L. Soule, Y. Niu, Y. Ding, H. Ding, D. Ding, M. Liu, An active and robust air electrode for reversible protonic ceramic electrochemical cells, ACS Energy Lett. 6(4) (2021) 1511-1520.https://doi.org/10.1021/acsenergylett.1c00432.

[10] K. Pei, Y. Zhou, K. Xu, H. Zhang, Y. Ding, B. Zhao, W. Yuan, K. Sasaki, Y. Choi, Y. Chen, M. Liu, Surface restructuring of a perovskite-type air electrode for reversible protonic ceramic electrochemical cells, Nat. Commun. 13(1) (2022) 2207.https://doi.org/10.1038/s41467-022-29866-5.

[11] C. Duan, R. Kee, H. Zhu, N. Sullivan, L. Zhu, L. Bian, D. Jennings, R. O'Hayre, Highly efficient reversible protonic ceramic electrochemical cells for power generation and fuel production, Nat. Energy 4(3) (2019) 230-240.https://doi.org/10.1038/s41560-019-0333-2.

[12] H. Ding, W. Wu, C. Jiang, Y. Ding, W. Bian, B. Hu, P. Singh, C.J. Orme, L. Wang, Y. Zhang, D. Ding, Self-sustainable protonic ceramic electrochemical cells using a triple conducting electrode for hydrogen and power production, Nat. Commun. 11(1) (2020) 1907.https://doi.org/10.1038/s41467-020-15677-z.

[13] Y. Zhou, W. Zhang, N. Kane, Z. Luo, K. Pei, K. Sasaki, Y. Choi, Y. Chen, D. Ding, M. Liu, An efficient bifunctional air electrode for reversible protonic ceramic electrochemical cells, Adv. Funct. Mater. 31(40) (2021) 2105386.https://doi.org/10.1002/adfm.202105386.

[14] F. Zhu, F. He, D. Liu, H. Zhang, Y. Xu, K. Xu, Y. Chen, A surface reconfiguration of a perovskite air electrode enables an active and durable reversible protonic ceramic electrochemical cell, Energy Storage Mater. 53 (2022) 754-762.https://doi.org/10.1016/j.ensm.2022.10.009.

[15] M. Liang, Y. Song, D. Liu, L. Xu, M. Xu, G. Yang, W. Wang, W. Zhou, R. Ran, Z. Shao, Magnesium tuned triple conductivity and bifunctionality of $BaCo_{0.4}Fe_{0.4}Zr_{0.1}Y_{0.1}O_{3-\delta}$ perovskite towards reversible protonic ceramic

electrochemical cells, Appl. Catal. B Environ. 318 (2022) 121868.https://doi.org/10.1016/j.apcatb.2022.121868.
[16] C. Duan, J. Huang, N. Sullivan, R. O'Hayre, Proton-conducting oxides for energy conversion and storage, Appl. Phys. Rev. 7(1) (2020).https://doi.org/10.1063/1.5135319.
[17] F. He, D. Song, R. Peng, G. Meng, S. Yang, Electrode performance and analysis of reversible solid oxide fuel cells with proton conducting electrolyte of $BaCe_{0.5}Zr_{0.3}Y_{0.2}O_{3-\delta}$, J. Power Sources 195(11) (2010) 3359-3364.https://doi.org/10.1016/j.jpowsour.2009.12.079.
[18] E. Fabbri, L. Bi, D. Pergolesi, E. Traversa, High-performance composite cathodes with tailored mixed conductivity for intermediate temperature solid oxide fuel cells using proton conducting electrolytes, Energy Environ. Sci. 4(12) (2011) 4984-4993.https://doi.org/10.1039/C1EE02361F.
[19] L. Yang, C. Zuo, S. Wang, Z. Cheng, M. Liu, A novel composite cathode for low-temperature SOFCs based on oxide proton conductors, Adv. Mater. 20(17) (2008) 3280-3283.https://doi.org/10.1002/adma.200702762.
[20] S. Lee, S. Park, S. Wee, H.w. Baek, D. Shin, One-dimensional structured $La_{0.6}Sr_{0.4}Co_{0.2}Fe_{0.8}O_{3-\delta}$ - $BaCe_{0.5}Zr_{0.35}Y_{0.15}O_{3-\delta}$ composite cathode for protonic ceramic fuel cells, Solid State Ionics 320 (2018) 347-352.https://doi.org/10.1016/j.ssi.2018.03.010.
[21] D. Ding, X. Li, S.Y. Lai, K. Gerdes, M. Liu, Enhancing SOFC cathode performance by surface modification through infiltration, Energy Environ. Sci. 7(2) (2014) 552-575.https://doi.org/10.1039/C3EE42926A.
[22] Y. Chen, Y. Choi, S. Yoo, Y. Ding, R. Yan, K. Pei, C. Qu, L. Zhang, I. Chang, B. Zhao, Y. Zhang, H. Chen, Y. Chen, C. Yang, B. deGlee, R. Murphy, J. Liu, M. Liu, A highly efficient multi-phase catalyst dramatically enhances the rate of oxygen reduction, Joule 2(5) (2018) 938-949.https://doi.org/10.1016/j.joule.2018.02.008.
[23] C. Duan, J. Tong, M. Shang, S. Nikodemski, M. Sanders, S. Ricote, A. Almansoori, R. O'Hayre, Readily processed protonic ceramic fuel cells with high performance at low temperatures, Science 349(6254) (2015) 1321-1326.https://doi.org/10.1126/science.aab3987.
[24] Y. Song, J. Liu, Y. Wang, D. Guan, A. Seong, M. Liang, M.J. Robson, X. Xiong, Z. Zhang, G. Kim, Z. Shao, F. Ciucci, Nanocomposites: a new opportunity for developing highly active and durable bifunctional air electrodes for reversible protonic ceramic cells, Adv. Energy Mater. 11(36) (2021) 2101899.https://doi.org/10.1002/aenm.202101899.
[25] Z. Tao, L. Bi, L. Yan, W. Sun, Z. Zhu, R. Peng, W. Liu, A novel single phase cathode material for a proton-conducting SOFC, Electrochem. Commun. 11(3) (2009) 688-690.https://doi.org/10.1016/j.elecom.2009.01.012.
[26] L. Yang, S. Wang, X. Lou, M. Liu, Electrical conductivity and electrochemical performance of cobalt-doped $BaZr_{0.1}Ce_{0.7}Y_{0.2}O_{3-\delta}$ cathode, Int. J. Hydrogen Energy 36(3) (2011) 2266-2270.https://doi.org/10.1016/j.ijhydene.2010.11.053.
[27] Y. Rao, S. Zhong, F. He, Z. Wang, R. Peng, Y. Lu, Cobalt-doped BaZrO3: a single phase air electrode material for reversible solid oxide cells, Int. J. Hydrogen Energy 37(17) (2012) 12522-12527.https://doi.org/10.1016/j.ijhydene.2012.05.022.
[28] C. Duan, R.J. Kee, H. Zhu, C. Karakaya, Y. Chen, S. Ricote, A. Jarry, E.J. Crumlin, D. Hook, R. Braun, N.P. Sullivan, R. O'Hayre, Highly durable, coking and sulfur tolerant, fuel-flexible protonic ceramic fuel cells, Nature 557(7704) (2018) 217-222.https://doi.org/10.1038/s41586-018-0082-6.
[29] Y. Song, Y. Chen, W. Wang, C. Zhou, Y. Zhong, G. Yang, W. Zhou, M. Liu, Z. Shao, Self-Assembled triple-conducting nanocomposite as a superior protonic ceramic fuel cell cathode, Joule 3(11) (2019) 2842-2853.https://doi.org/10.1016/j.joule.2019.07.004.
[30] D. Hu, J. Kim, H. Niu, L.M. Daniels, T.D. Manning, R. Chen, B. Liu, R. Feetham, J.B. Claridge, M.J. Rosseinsky, High-performance protonic ceramic fuel cell cathode using protophilic mixed ion and electron conducting material, J. Mater. Chem. A 10(5) (2022) 2559-2566.https://doi.org/10.1039/D1TA07113K.
[31] X. Xu, H. Wang, M. Fronzi, X. Wang, L. Bi, E. Traversa, Tailoring cations in a perovskite cathode for proton-

conducting solid oxide fuel cells with high performance, J. Mater. Chem. A 7(36) (2019) 20624-20632.https://doi.org/10.1039/C9TA05300J.
[32] S. Choi, C.J. Kucharczyk, Y. Liang, X. Zhang, I. Takeuchi, H.-I. Ji, S.M. Haile, Exceptional power density and stability at intermediate temperatures in protonic ceramic fuel cells, Nat. Energy 3(3) (2018) 202-210.https://doi.org/10.1038/s41560-017-0085-9.
[33] Z. Liu, D. Cheng, Y. Zhu, M. Liang, M. Yang, G. Yang, R. Ran, W. Wang, W. Zhou, Z. Shao, Robust bifunctional phosphorus-doped perovskite oxygen electrode for reversible proton ceramic electrochemical cells, Chem. Eng. J. 450 (2022) 137787.https://doi.org/10.1016/j.cej.2022.137787.
[34] R. Ren, Z. Wang, X. Meng, X. Wang, C. Xu, J. Qiao, W. Sun, K. Sun, Tailoring the oxygen vacancy to achieve fast intrinsic proton transport in a perovskite cathode for protonic ceramic fuel cells, ACS Appl. Energy Mater. 3(5) (2020) 4914-4922.https://doi.org/10.1021/acsaem.0c00486.
[35] N. Wang, H. Toriumi, Y. Sato, C. Tang, T. Nakamura, K. Amezawa, S. Kitano, H. Habazaki, Y. Aoki, $La_{0.8}Sr_{0.2}Co_{1-x}Ni_xO_{3-\delta}$ as the efficient triple conductor air electrode for protonic ceramic cells, ACS Appl. Energy Mater. 4(1) (2021) 554-563.https://doi.org/10.1021/acsaem.0c02447.
[36] M. Liang, F. He, C. Zhou, Y. Chen, R. Ran, G. Yang, W. Zhou, Z. Shao, Nickel-doped $BaCo_{0.4}Fe_{0.4}Zr_{0.1}Y_{0.1}O_{3-\delta}$ as a new high-performance cathode for both oxygen-ion and proton conducting fuel cells, Chem. Eng. J. 420 (2021) 127717.https://doi.org/10.1016/j.cej.2020.127717.
[37] Y. Li, Y. Li, Y. Wan, Y. Xie, J. Zhu, H. Pan, X. Zheng, C. Xia, Perovskite oxyfluoride electrode enabling direct electrolyzing carbon dioxide with excellent electrochemical performances, Adv. Energy Mater. 9(3) (2019) 1803156.https://doi.org/10.1002/aenm.201803156.
[38] J. Xiong, H. Zhong, J. Li, X. Zhang, J. Shi, W. Cai, K. Qu, C. Zhu, Z. Yang, S.P. Beckman, H. Cheng, Engineering highly active oxygen sites in perovskite oxides for stable and efficient oxygen evolution, Appl. Catal. B Environ. 256 (2019) 117817.https://doi.org/10.1016/j.apcatb.2019.117817.
[39] J. Gao, Y. Liu, Y. Gao, M. Yuan, Z. Wang, Z. Lü, Q. Li, B. Wei, Cobalt-free fluorine doped $Bi_{0.7}Sr_{0.3}FeO_{3-\delta}$ oxides for energetic cathodes of low-temperature solid oxide fuel cells, Chem. Eng. J. 452 (2023) 139584.https://doi.org/10.1016/j.cej.2022.139584.
[40] I.T. Bello, N. Yu, S. Zhai, Y. Song, S. Zhao, C. Cheng, Z. Zhang, M. Ni, Effect of engineered lattice contraction and expansion on the performance and CO_2 tolerance of $Ba_{0.5}Sr_{0.5}Co_{0.7}Fe_{0.3}O_{3-\delta}$ functional material for intermediate temperature solid oxide fuel cells, Ceram. Int. 48(15) (2022) 21416-21427.https://doi.org/10.1016/j.ceramint.2022.04.110.
[41] J. Xue, J. Li, L. Zhuang, L. Chen, A. Feldhoff, H. Wang, Anion doping CO_2-stable oxygen permeable membranes for syngas production, Chem. Eng. J. 347 (2018) 84-90.https://doi.org/10.1016/j.cej.2018.04.090.
[42] Y. Zhang, Z. Zhu, Y. Gu, H. Chen, Y. Zheng, L. Ge, Effect of Cl doping on the electrochemical performance of $Sr_2Fe_{1.5}Mo_{0.5}O_{6-\delta}$ cathode material for solid oxide fuel cells, Ceram. Int. 46(14) (2020) 22787-22796.https://doi.org/10.1016/j.ceramint.2020.06.046.
[43] Z. Zhang, Y. Zhu, Y. Zhong, W. Zhou, Z. Shao, Anion doping: a new strategy for developing high-performance perovskite-type cathode materials of solid oxide fuel cells, Adv. Energy Mater. 7(17) (2017) 1700242.https://doi.org/10.1002/aenm.201700242.
[44] P. Anitha Sukkurji, A. Molinari, C. Reitz, R. Witte, C. Kübel, V.S.K. Chakravadhanula, R. Kruk, O. Clemens, Anion doping of ferromagnetic thin films of $La_{0.74}Sr_{0.26}MnO_{3-\delta}$ via topochemical fluorination, Materials 11(7) (2018) 1204. https://doi.org/10.3390/ma11071204.
[45] Y. Xie, N. Shi, D. Huan, W. Tan, J. Zhu, X. Zheng, H. Pan, R. Peng, C. Xia, A Stable and Efficient Cathode for Fluorine-Containing Proton-Conducting Solid Oxide Fuel Cells, ChemSusChem 11(19) (2018) 3423-3430.https://doi.org/10.1002/cssc.201801193.

[46] J. Zhu, G. Liu, Z. Liu, Z. Chu, W. Jin, N. Xu, Unprecedented perovskite oxyfluoride membranes with high-efficiency oxygen ion transport paths for low-temperature oxygen permeation, Adv. Mater. 28(18) (2016) 3511-3515.https://doi.org/10.1002/adma.201505959.

[47] Y. Wan, Y. Xing, Y. Li, D. Huan, C. Xia, Thermal cycling durability improved by doping fluorine to $PrBaCo_2O_{5+\delta}$ as oxygen reduction reaction electrocatalyst in intermediate-temperature solid oxide fuel cells, J. Power Sources 402 (2018) 363-372.https://doi.org/10.1016/j.jpowsour.2018.09.065.

[48] Z. Ma, Q. Ye, B. Zhang, W. Yang, F. Dong, M. Ni, Z. Lin, A highly efficient and robust bifunctional perovskite-type air electrode with triple-conducting behavior for low-temperature solid oxide fuel cells, Adv. Funct. Mater. 32(47) (2022) 2209054.https://doi.org/10.1002/adfm.202209054.

[49] L. Zhang, W. Sun, C. Xu, R. Ren, X. Yang, J. Qiao, Z. Wang, K. Sun, Attenuating a metal–oxygen bond of a double perovskite oxide via anion doping to enhance its catalytic activity for the oxygen reduction reaction, J. Mater. Chem. A 8(28) (2020) 14091-14098.https://doi.org/10.1039/D0TA04820H.

[50] W. Wang, X. Zhang, D. Zhang, Q. Zeng, Y. Jiang, B. Lin, Highly promoted performance of triple-conducting cathode for YSZ-based SOFC via fluorine anion doping, Ceram. Int. 46(15) (2020) 23964-23971.https://doi.org/10.1016/j.ceramint.2020.06.173.

[51] Y. Chen, T. Hong, P. Wang, K. Brinkman, J. Tong, J. Cheng, Investigate the proton uptake process of proton/oxygen ion/hole triple conductor $BaCo_{0.4}Fe_{0.4}Zr_{0.1}Y_{0.1}O_{3-\delta}$ by electrical conductivity relaxation, J. Power Sources 440 (2019) 227122.https://doi.org/10.1016/j.jpowsour.2019.227122.

[52] N. Wang, C. Tang, L. Du, R. Zhu, L. Xing, Z. Song, B. Yuan, L. Zhao, Y. Aoki, S. Ye, Advanced cathode materials for protonic ceramic fuel cells: recent progress and future perspectives, Adv. Energy Mater. 12(34) (2022) 2201882.https://doi.org/10.1002/aenm.202201882.

[53] D. Poetzsch, R. Merkle, J. Maier, Stoichiometry variation in materials with three mobile carriers—thermodynamics and transport kinetics exemplified for protons, oxygen vacancies, and holes, Adv. Funct. Mater. 25(10) (2015) 1542-1557.https://doi.org/10.1002/adfm.201402212.

[54] R. Zohourian, R. Merkle, G. Raimondi, J. Maier, Mixed-conducting perovskites as cathode materials for protonic ceramic fuel cells: understanding the trends in proton uptake, Adv. Funct. Mater. 28(35) (2018) 1801241.https://doi.org/10.1002/adfm.201801241.

[55] R. Ren, X. Yu, Z. Wang, C. Xu, T. Song, W. Sun, J. Qiao, K. Sun, Fluorination inductive effect enables rapid bulk proton diffusion in $BaCo_{0.4}Fe_{0.4}Zr_{0.1}Y_{0.1}O_{3-\delta}$ perovskite oxide for high-activity protonic ceramic fuel cell cathode, Appl. Catal. B Environ. 317 (2022) 121759.https://doi.org/10.1016/j.apcatb.2022.121759.

[56] K. Belova, S. Baskakova, C. Argirusis, I. Animitsa, The effect of F^--doping on the conductivity of proton conductor $Ba_4Ca_2Nb_2O_{11}$, Electrochim. Acta 193 (2016) 63-71.https://doi.org/10.1016/j.electacta.2016.02.052.

[57] Y. Bu, S. Joo, Y. Zhang, Y. Wang, D. Meng, X. Ge, G. Kim, A highly efficient composite cathode for proton-conducting solid oxide fuel cells, J. Power Sources 451 (2020) 227812.https://doi.org/10.1016/j.jpowsour.2020.227812.

[58] T. Hu, F. Zhu, J. Xia, F. He, Z. Du, Y. Zhou, Y. Liu, H. Wang, Y. Chen, In situ engineering of a cobalt-free perovskite air electrode enabling efficient reversible oxygen reduction/evolution reactions, Adv. Funct. Mater. n/a(n/a) (2023) 2305567.https://doi.org/10.1002/adfm.202305567.

[59] Y. Zhang, B. Chen, D. Guan, M. Xu, R. Ran, M. Ni, W. Zhou, R. O'Hayre, Z. Shao, Thermal-expansion offset for high-performance fuel cell cathodes, Nature 591(7849) (2021) 246-251.https://doi.org/10.1038/s41586-021-03264-1.

[60] K. Xu, H. Zhang, Y. Xu, F. He, Y. Zhou, Y. Pan, J. Ma, B. Zhao, W. Yuan, Y. Chen, M. Liu, An efficient steam-induced heterostructured air electrode for protonic ceramic electrochemical cells, Adv. Funct. Mater. 32(23) (2022) 2110998.https://doi.org/10.1002/adfm.202110998.

[61] C. Zhou, D. Liu, M. Fei, X. Wang, R. Ran, M. Xu, W. Wang, W. Zhou, R. O'Hayre, Z. Shao, Cathode water management towards improved performance of protonic ceramic fuel cells, J. Power Sources 556 (2023) 232403.https://doi.org/10.1016/j.jpowsour.2022.232403.
[62] R. Ren, Z. Wang, C. Xu, W. Sun, J. Qiao, D.W. Rooney, K. Sun, Tuning the defects of the triple conducting oxide $BaCo_{0.4}Fe_{0.4}Zr_{0.1}Y_{0.1}O_{3-\delta}$ perovskite toward enhanced cathode activity of protonic ceramic fuel cells, J. Mater. Chem. A 7(31) (2019) 18365-18372.https://doi.org/10.1039/C9TA04335G.

Support Information

Facile Anion Engineering: A Pathway to Realizing Enhanced Triple Conductivity in Oxygen Electrodes for Reversible Protonic Ceramic Electrochemical Cells

S1. Experiment Section

S1.1 Powders synthesis

The nominal oxygen electrodes powders ($Ba_{0.5}Sr_{0.5}Co_{0.8}Fe_{0.2}X_{0.1}O_{2.9-\delta}$ (BSCF(F/C), x = O, F, Cl)) are prepared through the method of sol–gel EDTA-citric acid (CA) complexing as previously described[1, 2]. The difference is that the desired powers were obtained by calcining the precursors at 950°C for 5 hours in air.

In addition, the synthesis process of proton-conducting $BaZr_{0.1}Ce_{0.7}Y_{0.1}Yb_{0.1}O_{3-\delta}$ (BZCYYb) electrolyte powder is similar with above mentioned approach, with the distinction being the chemical reagents used (the corresponding metal nitrates) and the sintering temperature (1050°C for 5 hours).

S1.2 Cells fabrication

Here, the electrochemical catalytical performance of the oxygen electrode materials are evaluated by fabricating the BZCYYb electrolyte supported symmetrical cells with a configuration of BSCF(F/C)|BZCYYb|(BSCF(F/C). Specifically, the synthesized powder (BZCYYb) was initially weighed and pressed uniaxially into disc-shaped pellets, which were then sintered at 1400 °C for 10 h to make it dense. The cathode slurry (compositions shown in Table S1), which is prepared by mixing the calcined oxygen electrode powder with glycol, isopropyl alcohol, and ethylene glycerol to form a homogeneous suspension, was used to

uniformly spray on both surfaces of the dense electrolyte pellets, and then co-calcined at 900 °C for 2 h in ambient air. In the end, silver paste was applied on the surface of both sides cathodes as the current collector to successfully fabricated the symmetrical cell to conduct the electrochemical tests.

At the same time, the hydrogen electrode supported single cells were also fabricated with a configuration of NiO-BZCYYb|BZCYYb|BSCF(F/Cl) to investigate the electricity/hydrogen generation performance. Regarding the preparation of the electrochemical cells, firstly, ball mixing BZCYYb, NiO and soluble starch powders (compositions shown in Table S1) with pure ethanol for 2 h to obtain the hydrogen electrode power, and then dried in 130 °C. About 0.35g of the collected dry powders was weighed and then pressed into pellet at a uniaxial pressure of 1 Mpa. After that, a mass of around 0.015g BZCYYb electrolyte powder was spread uniformly on the surface of the pressed hydrogen electrode, followed by co-pressing under a pressure of 2 Mpa. The co-pressed pellets were then calcined at 1450 °C for 5h in air, and the double-layer pellets with dense electrolyte and porous hydrogen electrode were obtained. Finally, the oxygen electrode is introduced by spray depositing the prepared slurry on the surface of BZCYYb electrolyte and processing another sintering at 900 °C for 2 h in air.

S1.3 Materials characterization

X-ray diffraction (XRD, Rigaku SmartLab 9kW) was used to examine the phase compositions of the as-synthesized BZCYYb electrolyte and BSCF, BSCFF and BSCFC air electrode powders. The diffraction patterns were collected by setting a step-scan model in the range of 20-80° with an interval of 0.02°. The refinement of the obtained XRD results was achieved by

using the Opensource Fullprof Suite software to disclose more details about the prepared oxygen electrode materials crystal structures. The microstructure and elements distribution of the calcined oxygen electrode powders was probed using high-resolution transmission microscopy (HR-TEM, America, FEI Tecnai F20) with an energy dispersive X-ray spectrometer (EDX) device. The concentration of oxygen vacancies ($V_O^{\cdot\cdot}$) of the air electrodes was determined by the iodometric titration method that reported previously[3-5]. At the same time, the thermodynamic mass loss curves were conducted to estimate $V_O^{\cdot\cdot}$ at high temperature by thermogravimetric analysis (Germany, Netzsch TG 209 F3 Tarsus) under flowing synthetic air from room temperature to 900 ºC with a heating rate of 10 ºC min^{-1}. The oxygen temperature programmed desorption (O_2-TPD) technique was carried out to measure the oxygen desorption properties of the air electrodes materials in the temperature range of 100-900 ºC. The valence state of the oxygen and metal elements in the powders at room temperature was analyzed by the X-ray photoelectron spectroscopy (XPS, Thermo Fisher Scientific Nexsa) with a monochromatic Al Kα radiation. The microstructure of the fabricated single cells was observed by the scanning electron microscopy (SEM, TESCAN MAIA3). The electrical conductivity relaxation (ECR) curves and electrical conductivity results were obtained through a four-probe DC configuration (Keithley 2440 source meter). The ECR data, which is obtained by switching the oxygen partial pressure of the testing atmosphere, was applied to determine the surface exchange kinetics (K_{chem}) and the bulk diffusion coefficient (D_{chem}) for oxygen fitted by ECR tools, and more datils about the ECR procedure related to oxygen can be found elsewhere[6-9]. Moreover, the similar ECR procedure was also conducted by switching the water partial pressure to determine the proton mobility ability of these air electrodes, and the mechanism

and calculated processes were reported previously[10, 11].

S1.4 Electrochemical measured

The polarization resistance of the symmetrical cells is measured by the electrochemical impedance spectroscopy (EIS) using Solarton 1260 and Solarton 1287 equipment within the temperature range of 450-650°C. Nyquist plots were obtained under open circuit voltage (OCV) conditions with a 20 mV AC amplitude in the frequency range of 10^6 to 10^{-1} Hz. The gas flow rate was maintained at 100 ml/min throughout the experiments.

The i-V-p curves of the hydrogen electrode-supported single cell are obtained using a four-probe configuration with the help of Keithley 2440 source meter equipment, covering the temperature range of 450-650°C. EIS results were obtained using the aforementioned Solarton equipment to determine the ohmic and polarization resistance with a 20 mV AC amplitude in the frequency range of 10^6 to 10^{-1} Hz. During fuel cell operation, the hydrogen side was supplied with pure H_2 (50 ml/min), while the oxygen electrode was exposed to ambient air. In the electrolysis operation mode, the hydrogen side continued to receive the same gas (dry hydrogen) as mentioned in the fuel cell mode, while the atmosphere of the oxygen electrode was switched to wet air (3% H_2O-air) at a flow rate of 100 ml/min.

S1.5 Computational details

All spin-polarized density functional theory (DFT) calculations for periodic material systems were performed with the Vienna Ab initio simulation package (VASP)[12] using the projector-augmented wave (PAW) method[13]. The exchange–correlation function was handled using the generalized gradient approximation (GGA) formulated by the Perdew-Burke-Ernzerhof

(PBE). An effective U value of 4.0 eV for Fe and 3.3 eV for Co were determined using the Hubbard U model (DFT + U)[14]. The van der Waals (vdW) interactions are described with the DFT-D3 method in Grimme's scheme. The interaction between the atomic core and electrons was described by the projector augmented wave method. The plane-wave basis set energy cutoff was set to 500 eV[15-17]. The Brillouin zone was sampled with a 3 × 3 × 1 grid centered at the gamma (Γ) point for geometry relaxation. All the slabbed models possessed a vacuum spacing of ≈15 A˚ sampled, ensuring negligible lateral interaction of adsorbates. The bottom layers about half of the structure were kept frozen at the lattice position. All structures with a dynamic magnetic moment were fully relaxed to optimize without any restriction until their total energies were converged to $< 1\times10^{-6}$ eV, and the average residual forces were < 0.02 eV/Å.

S2. Supporting Figures

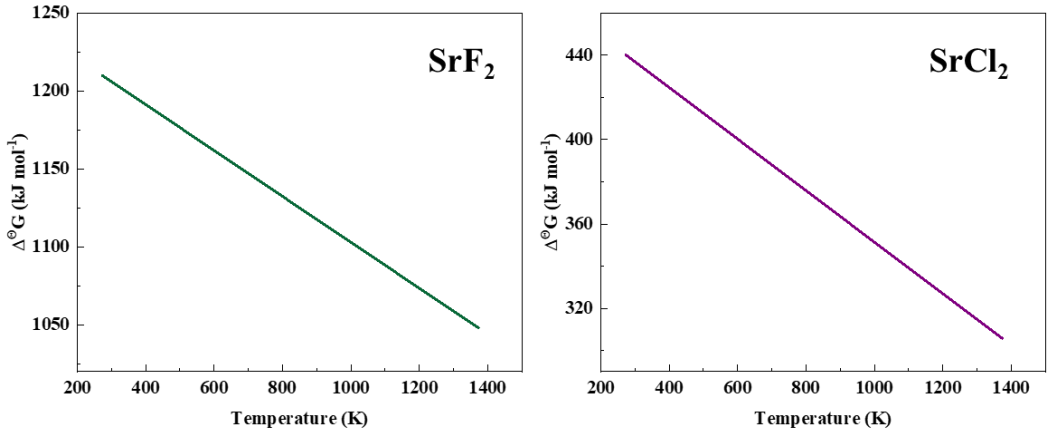

Fig. S1 The standard Gibbs free energy change ($\Delta^{\ominus}G$, kJ·mol^{-1}) of reactions (a) $2SrF_2+O_2 \rightarrow 2SrO+2F_2$ and (b) $2SrF_2+O_2 \rightarrow 2SrO+2F_2$. The positively high value of ($\Delta^{\ominus}G$) means the reactions are hard to conduct, which indicates the doping F^- and Cl^- is stable in this composite after high-temperature sintering.

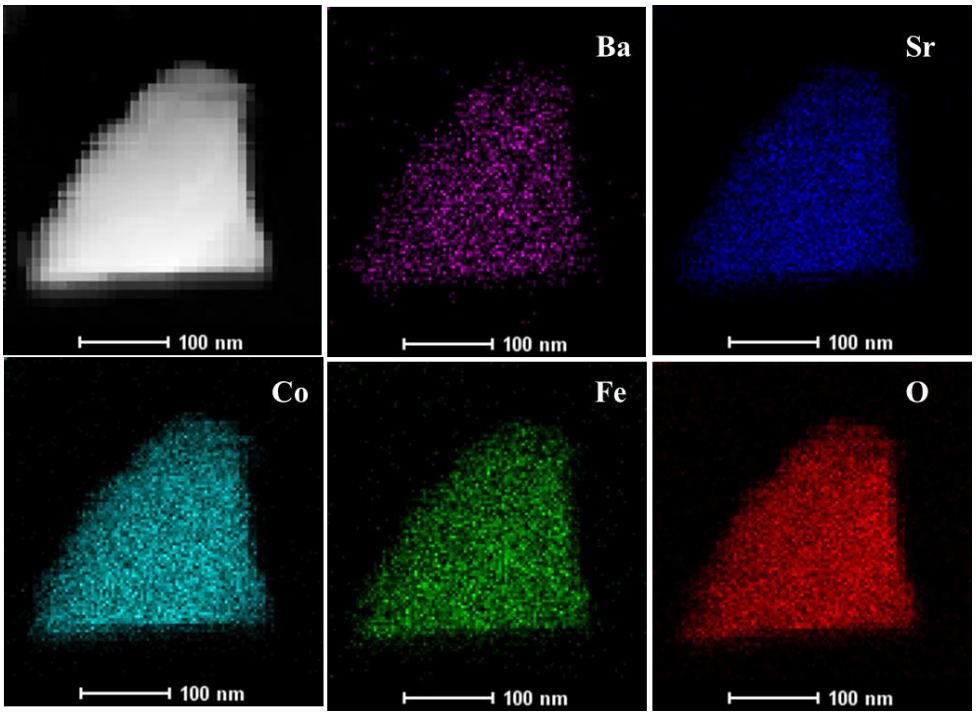

Fig. S2 The elements distribution of BSCF powder after sintering at 1000 °C for 5 hours.

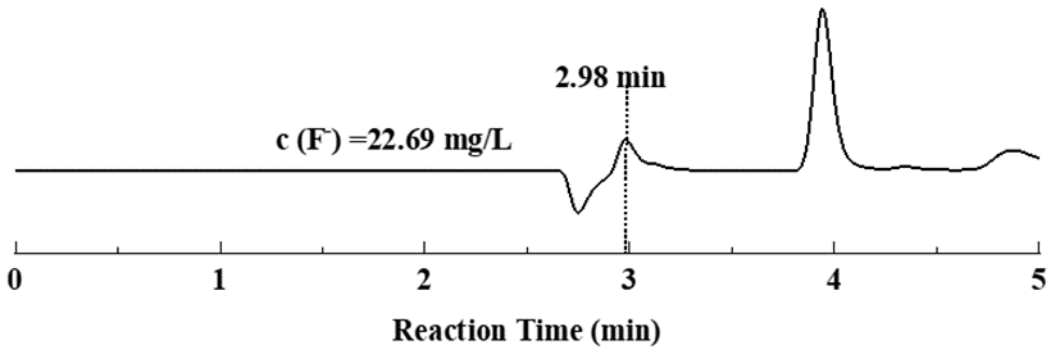

Fig.S3 Ion chromatogram of as-prepared BSCFF solutions (2.5 g/L).

Note: the calculated value of the mass percentage of fluorine is 0.91%, in line with the targeted value of 0.89%.

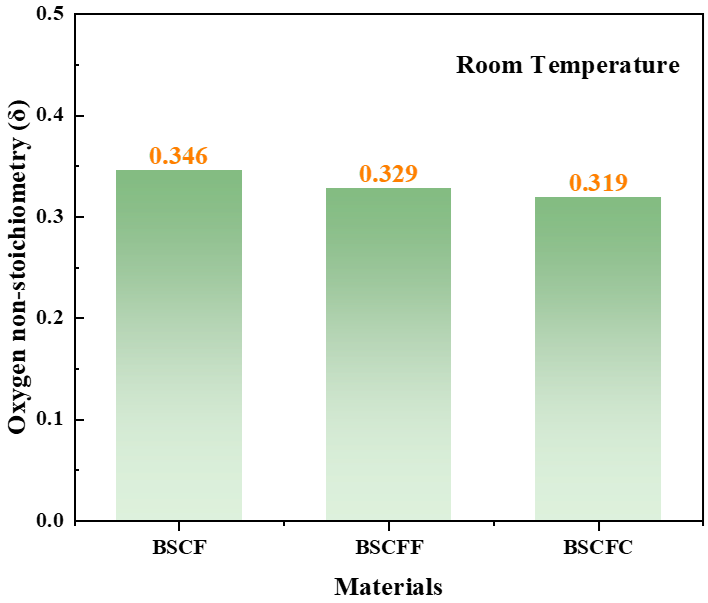

Fig. S4 The oxygen non-stoichiometry of the BSCF, BSCFF, and BSCFC samples at room temperature determined by iodometric titration.

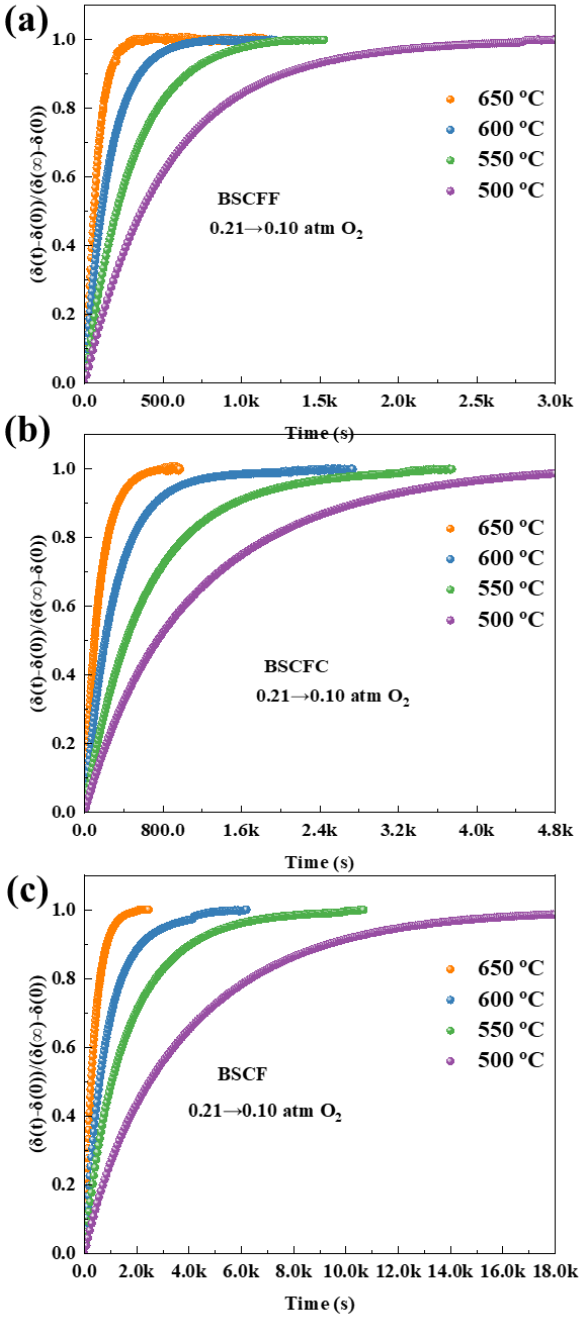

Fig. S5 Normalized conductivity curves for (a) BSCFF, (b) BSCFC and (c) BSCF samples when change the oxygen partial pressure from 0.21 atm to 0.1 atm at the temperatures rang from 650 °C to 500 °C.

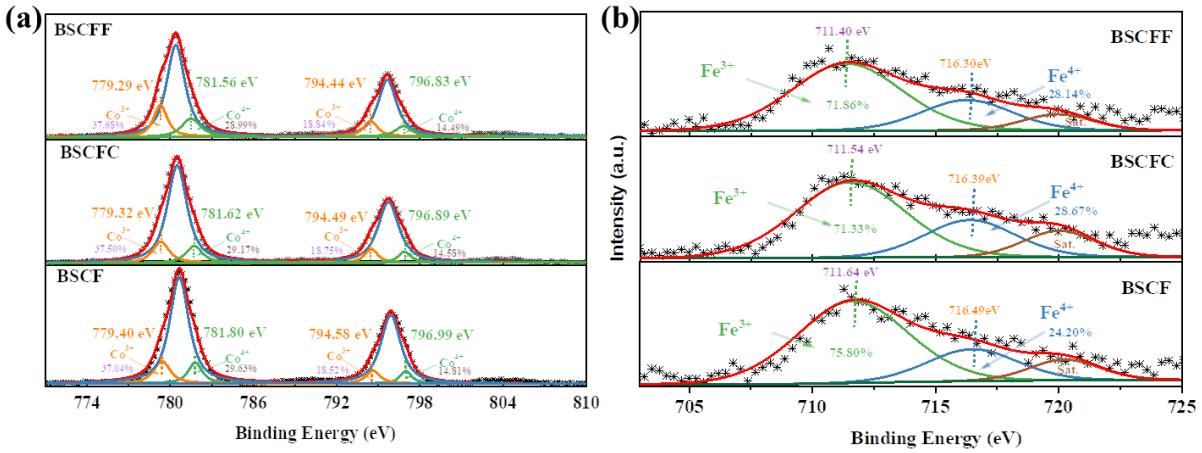

Fig. S6 the XPS spectra of (a) Co 2p (yellow and green lines) and Ba 3d (blue lines); and (b) Fe 2p (green and blue lines) for BSCF, BSCFC and BSCFF samples.

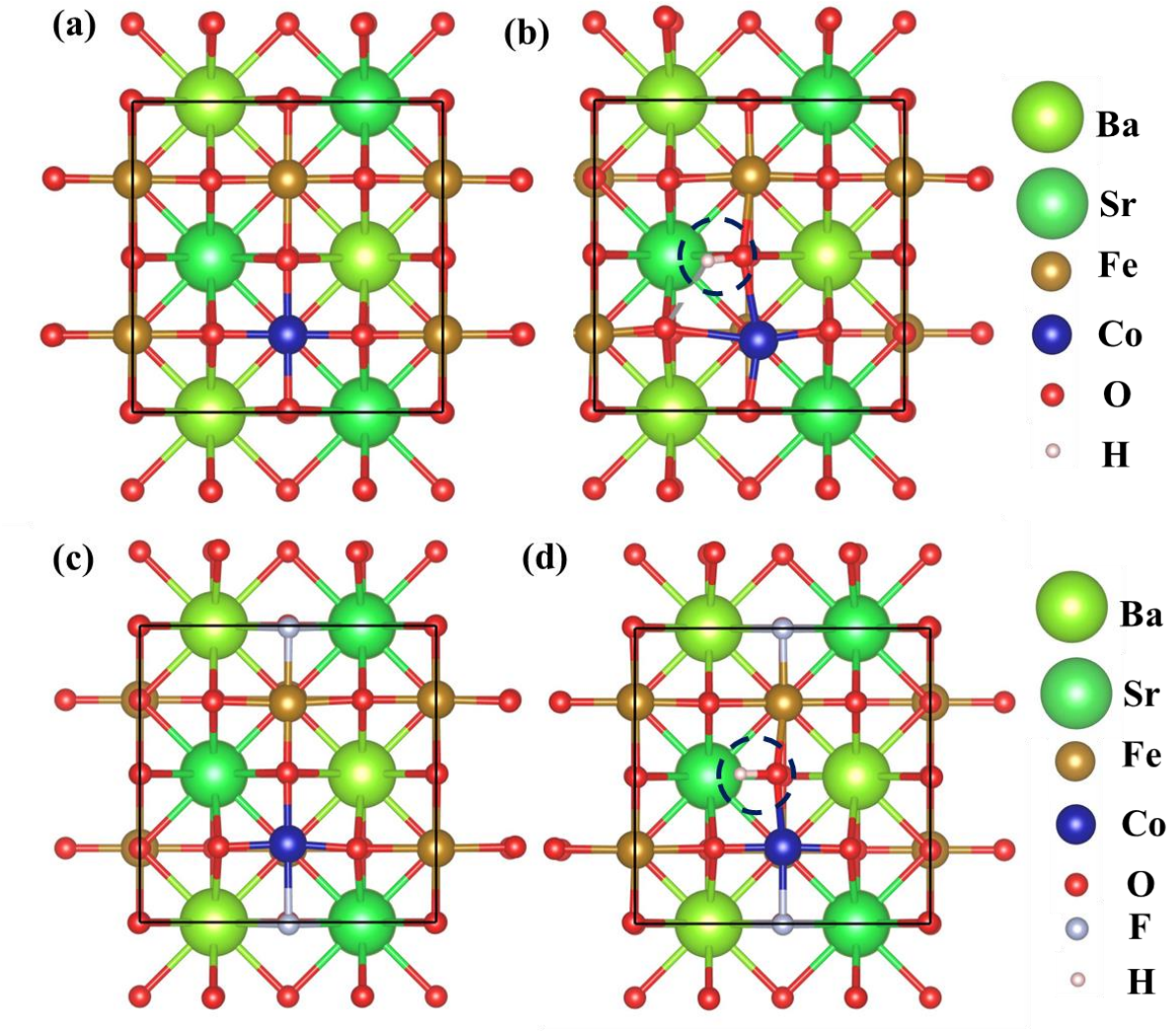

Fig S7 Schematic diagrams of the cell structures of (a, b) BSCF and (c, d) BSCFF samples (a, c) before and (b, d) after proton adsorption.

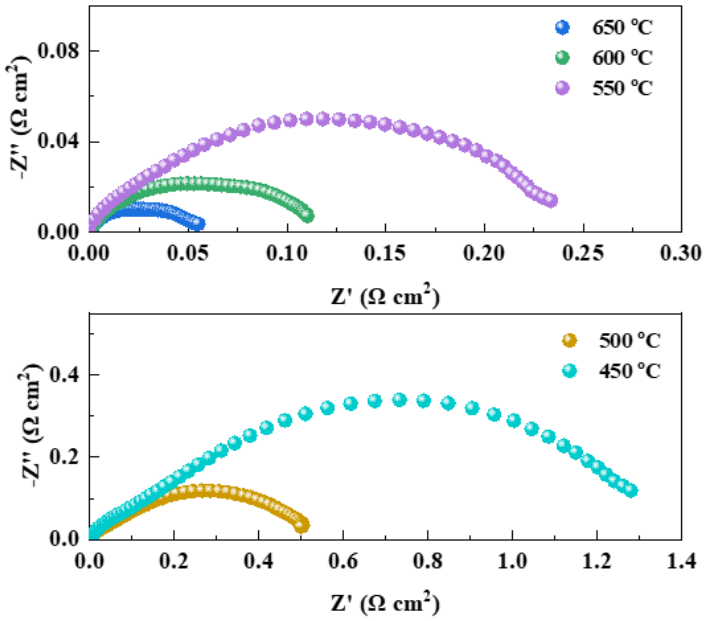

Fig. S8 Nyquist plots for BSCFF samples as a configuration of BSCFF|BZCYYb|BSCFF in wet air at 650-450 °C.

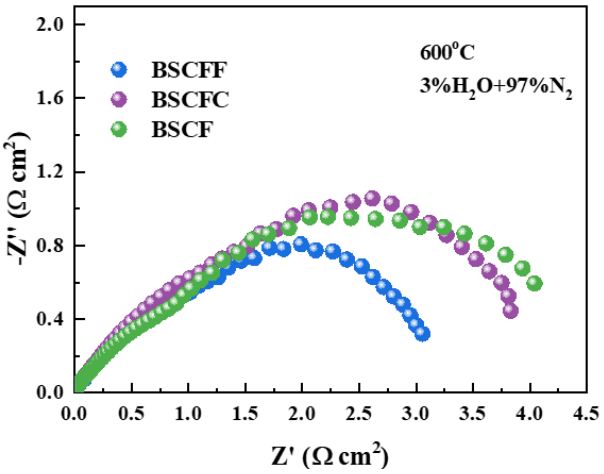

Fig. S9 Nyquist plots for BSCF, BSCFC and BSCFF electrodes assembled as symmetrical cells in wet N_2 at 600 °C.

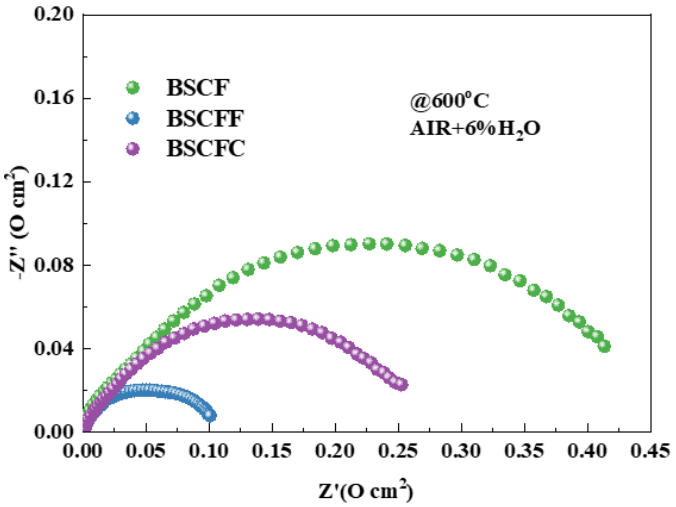

Fig. S10 Nyquist plots for BSCF, BSCFC and BSCFF electrodes assembled as symmetrical cells in 6%H_2O+air atmosphere at 600 °C.

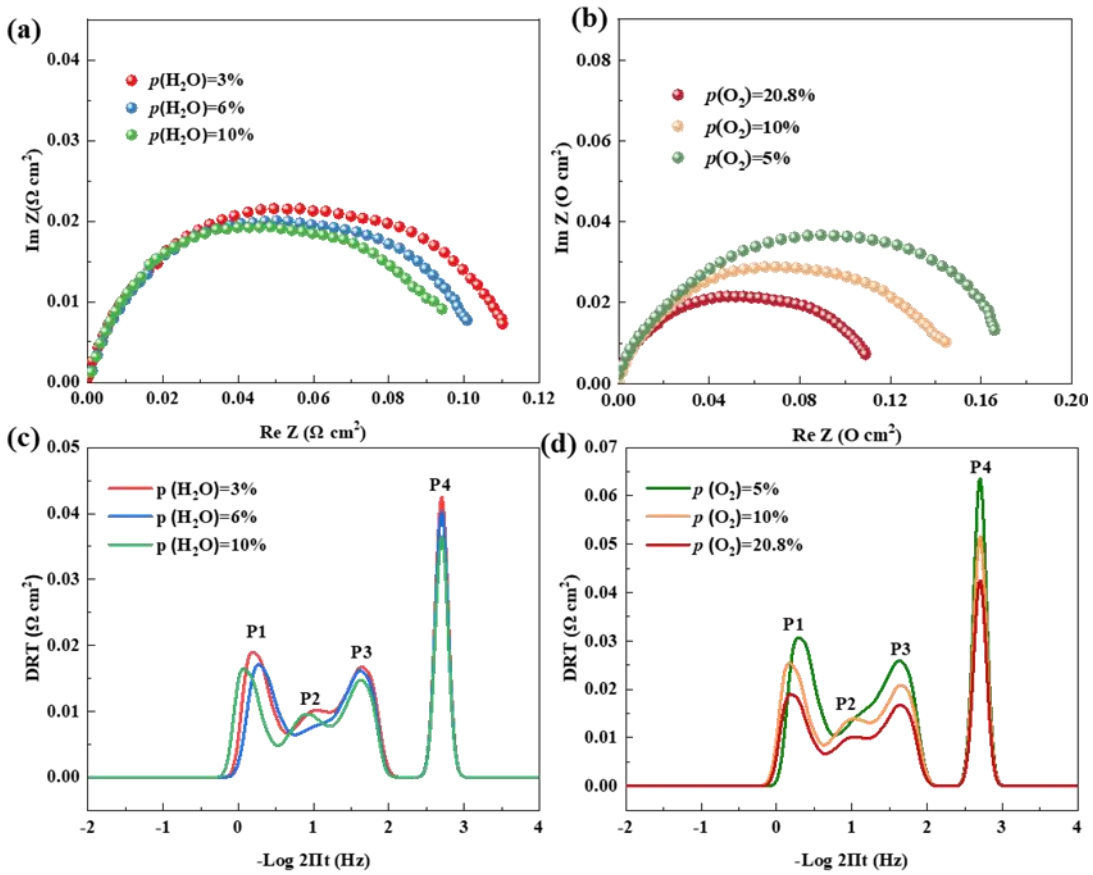

Fig. S11 The comparison of (a, b) Nyquist plots and (c, d) DRT plots of BSCFF air electrode in different (a, c) *p*H2O and (b, d) *p*O2 atmospheres operating at 600 °C.

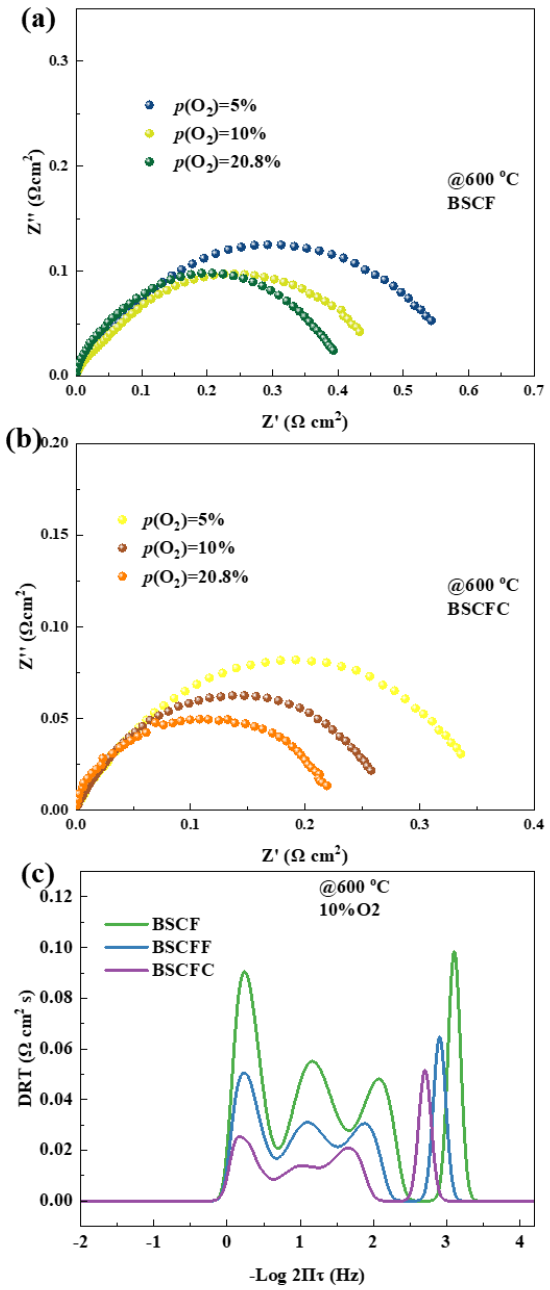

Fig. S12 Nyquist plots for (a)BSCF and (b) BSCFC samples with different O_2 partial pressure; (c) the comparison of DRT plots in humid 10%O_2 atmosphere at 600 °C.

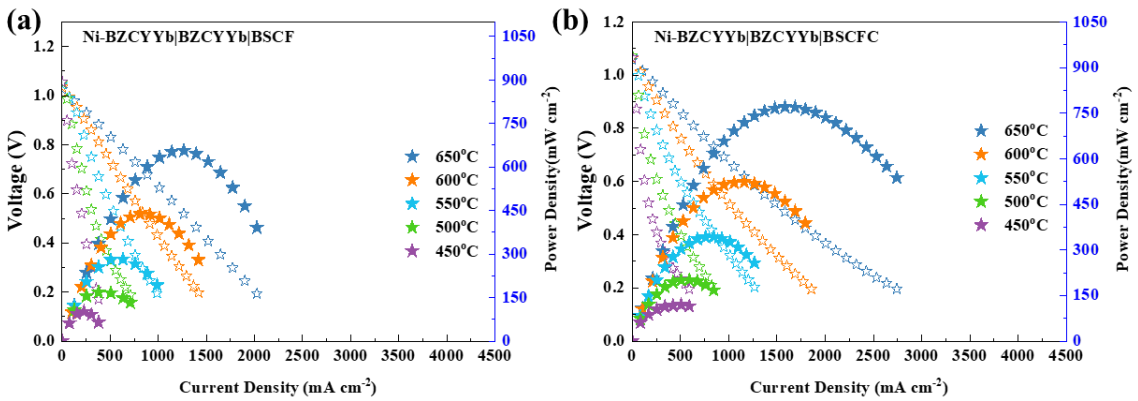

Fig. S13 The typic i-V-p curves of the NiO-BZCYYb anode supported single cell using H_2 as fuel and air as oxidant with (a) BSCF and (b) BSCFC cathodes at the elapsed temperatures range from 650 °C to 450 °C.

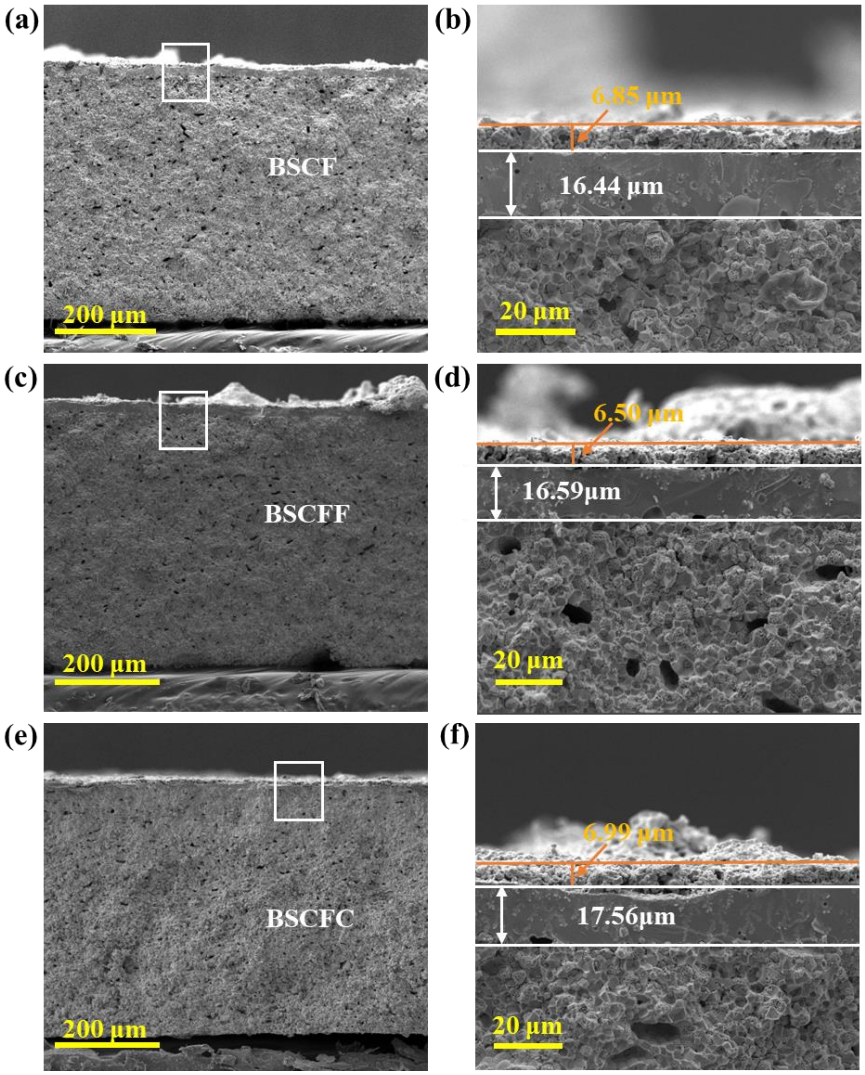

Fig. S14 The SEM images of (a,c,e) the cross section and (b,d,e) the enlarge part about the cathode and electrolyte layers of the test single cell with (a,b) BSCF, (c,d) BSCFF and (e,f) BSCFC cathodes

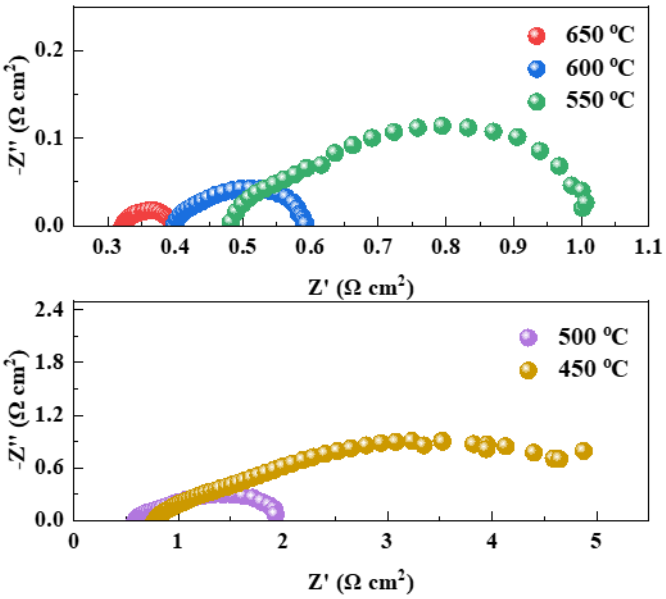

Fig. S15 The Nyquist plots of the NiO-BZCYYb anode supported single cell using H_2 as fuel and air as oxidant with BSCFF cathode at the elapsed temperatures range from 650 ºC to 450 ºC.

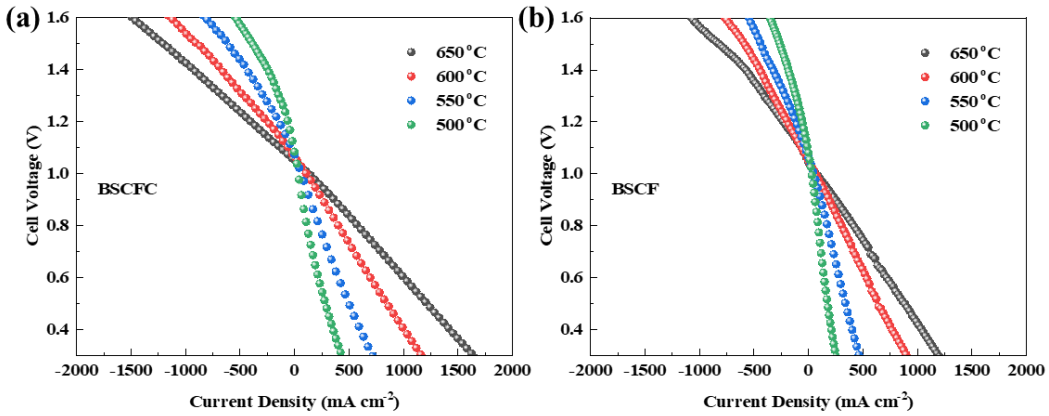

Fig. S16 The i-V curves of the RePCCS using H_2 as fuel and wet air as oxidant with (a) BSCFC and (b) BSCF air electrodes at the elapsed temperatures range from 650 ºC to 500 ºC.

S3. Supporting Tables

Table. S1 The compositions of the cathode slurry and hydrogen electrode

	composition	weight (%)
cathode	BSCF(F/C)	5.3
	glycol	15.1
	isopropyl alcohol	75.8
	ethylene glycerol	3.8
anode	NiO	31.8
	BZCYYb	59.1
	starch	9.0

Table. S2 Fitting results of BSCF, BSCFC and BSCFF of the O 1s XPS spectra

Sample	Relative Proportion		
	O^{2-}	O_2^{2-}/O^-	O_2/OH^-
BSCF	10.56%	27.33%	62.11%
BSCFC	24.48%	31.34%	44.18%
BSCFF	23.78%	31.20%	45.02%

Table. S3 The fitting D_{chem} and K_{chem} values for BSCF, BSCFC and BSCFC bar-samples at different temperatures and their corresponding activation energy (Ea)

Samples	Temperature (K)	D_{chem} (cm^2 s^{-1})	K_{chem} (cm s^{-1})	Ea for D_{chem}(kJ/mol)	Ea for K_{chem}(kJ/mol)
BSCF	873.15	0.21×10^{-5}	0.20×10^{-4}	92.08	93.14
	923.15	0.48×10^{-5}	0.47×10^{-4}		
	973.15	0.90×10^{-5}	0.90×10^{-4}		
	1023.15	2.24×10^{-5}	2.28×10^{-4}		
BSCFC	873.15	0.66×10^{-5}	0.66×10^{-4}	82.55	83.34
	923.15	1.20×10^{-5}	1.21×10^{-4}		
	973.15	2.50×10^{-5}	2.52×10^{-4}		
	1023.15	5.31×10^{-5}	5.40×10^{-4}		
BSCFF	873.15	2.30×10^{-5}	2.35×10^{-4}	79.17	81.59
	923.15	4.38×10^{-5}	4.55×10^{-4}		
	973.15	8.20×10^{-5}	8.49×10^{-4}		
	1023.15	17.4×10^{-5}	19.1×10^{-4}		

Table. S4 Comparison of ASR values for the state-of-art air electrodes based on BZCYYb electrolyte supported symmetrical cells in wet air.

Air Electrode	ASR (Ω cm^2)							Reference
	Temperature (^{o}C)							
	750	700	650	600	550	500	450	
BSCFF			0.06	0.12	0.25	0.54	1.41	This Work
BSCFC			0.10	0.23	0.53	1.37	4.37	This Work
BSCF			0.17	0.41	1.14	3.97	16.09	This Work
BCFZY	0.097	0.17	0.35	0.62	1.05	1.83		12
PBSCF	0.079	0.12	0.23	0.8				13
BCFZ			0.6	1.02	1.88	3.85	8.4	14
LSCF		0.09	0.23	0.50	1.41	3.83		15
BCO-LSCF		0.04	0.08	0.17	0.37	0.84		15
SCFN			0.08	0.20	0.58	1.98	8.35	16
BCCY			0.08	0.25	0.49	1.40	4.76	17

*BCFZY[18]: $BaCo_{0.4}Fe_{0.4}Zr_{0.1}Y_{0.1}O_{3-\delta}$; PBCFN[19]: $PrBaCo_{1.6}Fe_{0.2}Nb_{0.2}O_{5+\delta}$; BCFZ[20]: $BaCo_{0.4}Fe_{0.4}Zr_{0.2}O_{3-\delta}$; LSCF[21]: $La_{0.6}Sr_{0.4}Co_{0.2}Fe_{0.8}O_{3-\delta}$; BCO-LSCF[21]: barium cobaltite (BCO) coated LSCF; SCFN[22]: $Sr_{0.9}Ce_{0.1}Fe_{0.8}Ni_{0.2}O_{3-\delta}$; BCCY[23]: self-assembled $BaCo_{0.7}(Ce_{0.8}Y_{0.2})_{0.3}O_{3-\delta}$.

Table. S5 Comparison of peak power densities (PPDs) between the PCFCs with the BSCFF as the air electrode and the PCFCs with state-of-the-art air electrodes.

Air Electrode	PPD (mW cm^{-2})					Reference
	Temperature (°C)					
	650	600	550	500	450	
BSCFF	977	668	472	302	215	This Work
PNC		528	354	230		18
BCCY	985	743	508	319	187	17
SCFN	745	531	347	225		16
SEFC	350.2	0.8				19
RP-SF	530	372	253	144		20
PBCC95		540	354	222		21
BaCFBi	551	372	253	144		22
BCFZY	580	482	398	278		23

*PNC[24]: $PrNi_{0.5}Co_{0.5}O_{3-\sigma}$; BCCY[23]: $BaCo_{0.7}(Ce_{0.8}Y_{0.2})_{0.3}O_{3-\delta}$; SCFN[22]: $Sr_{0.9}Ce_{0.1}Fe_{0.8}Ni_{0.2}O_{3-\delta}$; SEFC[25]: $SrEu_2Fe_{1.8}Co_{0.2}O_{7-\delta}$; RP-SF[26]: $Sr_3Fe_2O_{7-\sigma}$; PBCC95[27]: $(PrBa_{0.8}Ca_{0.2})_{0.95}Co_2O_{6-\delta}$; BCFBi[28]: $BaCe_{0.5}Fe_{0.3}Bi_{0.2}O_{3-\delta}$; BCFZY[29]: $BaCo_{0.4}Fe_{0.4}Zr_{0.1}Y_{0.1}O_{3-\sigma}$.

Table. S6 Comparison of electrolysis current (EA) between PCECs with BSCFF as air electrode, and PCECs with state-of-the-art air electrodes.

Air Electrode	**Current Density (mA cm^{-2})**	Reference
BSCFF	590	This Work
BSCFC	485	This Work
BCSF	327	This Work
SCFN	364	16
SEFC	414	19
SEF	237	19
LSN	83	24
SSC	210	25
BGLC	119	26
PNO	360	27

*SCFN[22]: $Sr_{0.9}Ce_{0.1}Fe_{0.8}Ni_{0.2}O_{3-\delta}$; SEFC[25]: $SrEu_2Fe_{1.8}Co_{0.2}O_{7-\delta}$; SEF[25]: $SrEu_2Fe_2O_{7-\delta}$; LSN)[30]: $La_{1.2}Sr_{0.8}NiO_4$; SSC[31]: $Sm_{0.5}Sr_{0.5}CoO_{3-\delta}$; BGLC[32]: $BaGd_{0.8}La_{0.2}Co_2O_{6-\delta}$; PNO[33]: $Pr_2NiO_{4+\delta}$.

References

[1] M. Liang, Y. Zhu, Y. Song, D. Guan, Z. Luo, G. Yang, S.P. Jiang, W. Zhou, R. Ran, Z. Shao, A new durable surface nanoparticles-modified perovskite cathode for protonic ceramic fuel cells from selective cation exsolution under oxidizing atmosphere, Adv. Mater. 34(10) (2022) 2106379.https://doi.org/10.1002/adma.202106379.

[2] I.T. Bello, N. Yu, Y. Song, J. Wang, T.-S. Chan, S. Zhao, Z. Li, Y. Dai, J. Yu, M. Ni, Electrokinetic insights into the triple Ionic and electronic conductivity of a novel nanocomposite functional material for protonic ceramic fuel cells, Small 18(40) (2022) 2203207.https://doi.org/10.1002/smll.202203207.

[3] Z. Zhang, Y. Zhu, Y. Zhong, W. Zhou, Z. Shao, Anion doping: a new strategy for developing high-performance perovskite-type cathode materials of solid oxide fuel cells, Adv. Energy Mater. 7(17) (2017) 1700242.https://doi.org/10.1002/aenm.201700242.

[4] Y. Wang, L. Chen, H. Cao, Z. Chi, C. Chen, X. Duan, Y. Xie, F. Qi, W. Song, J. Liu, S. Wang, Role of oxygen vacancies and Mn sites in hierarchical Mn_2O_3/$LaMnO_{3-\delta}$ perovskite composites for aqueous organic pollutants decontamination, Appl. Catal. B Environ. 245 (2019) 546-554.https://doi.org/10.1016/j.apcatb.2019.01.025.

[5] K. Chu, F. Liu, J. Zhu, H. Fu, H. Zhu, Y. Zhu, Y. Zhang, F. Lai, T. Liu, A general strategy to boost electrocatalytic nitrogen reduction on perovskite oxides via the oxygen vacancies derived from A-site deficiency, Advanced Energy Materials 11(11) (2021) 2003799.https://doi.org/10.1002/aenm.202003799.

[6] A. Seong, J. Kim, D. Jeong, S. Sengodan, M. Liu, S. Choi, G. Kim, Electrokinetic proton transport in triple ($H^+/O^{2-}/e^-$) conducting oxides as a key descriptor for highly efficient protonic ceramic fuel cells, Adv. Sci. 8(11) (2021) 2004099.https://doi.org/10.1002/advs.202004099.

[7] D. Liu, Y. Dou, T. Xia, Q. Li, L. Sun, L. Huo, H. Zhao, B-site La, Ce, and Pr-doped $Ba_{0.5}Sr_{0.5}Co_{0.7}Fe_{0.3}O_{3-\delta}$ perovskite cathodes for intermediate-temperature solid oxide fuel cells: Effectively promoted oxygen reduction activity and operating stability, J. Power Sources 494 (2021) 229778.https://doi.org/10.1016/j.jpowsour.2021.229778.

[8] D. Chen, Z. Shao, Surface exchange and bulk diffusion properties of $Ba_{0.5}Sr_{0.5}Co_{0.8}Fe_{0.2}O_{3-\delta}$ mixed conductor, Int. J. Hydrogen Energy 36(11) (2011) 6948-6956.https://doi.org/10.1016/j.ijhydene.2011.02.087.

[9] Y. Chen, T. Hong, P. Wang, K. Brinkman, J. Tong, J. Cheng, Investigate the proton uptake process of proton/oxygen ion/hole triple conductor $BaCo_{0.4}Fe_{0.4}Zr_{0.1}Y_{0.1}O_{3-\delta}$ by electrical conductivity relaxation, J. Power Sources 440 (2019) 227122.https://doi.org/10.1016/j.jpowsour.2019.227122.

[10] R. Ren, X. Yu, Z. Wang, C. Xu, T. Song, W. Sun, J. Qiao, K. Sun, Fluorination inductive effect enables rapid bulk proton diffusion in $BaCo_{0.4}Fe_{0.4}Zr_{0.1}Y_{0.1}O_{3-\delta}$ perovskite oxide for high-activity protonic ceramic fuel cell cathode, Appl. Catal. B Environ. 317 (2022) 121759.https://doi.org/10.1016/j.apcatb.2022.121759.

[11] R. Ren, Z. Wang, X. Meng, X. Wang, C. Xu, J. Qiao, W. Sun, K. Sun, Tailoring the oxygen vacancy to achieve fast intrinsic proton transport in a perovskite cathode for protonic ceramic fuel cells, ACS Appl. Energy Mater. 3(5) (2020) 4914-4922.https://doi.org/10.1021/acsaem.0c00486.

[12] G. Kresse, J. Furthmüller, Efficiency of ab-initio total energy calculations for metals and

semiconductors using a plane-wave basis set, Comput. Mater. Sci. 6(1) (1996) 15-50.https://doi.org/10.1016/0927-0256(96)00008-0.
[13] P.E. Blöchl, Projector augmented-wave method, Phys.Rev.B. 50(24) (1994) 17953-17979.https://doi.org/10.1103/PhysRevB.50.17953.
[14] Y. Sun, H. Liao, J. Wang, B. Chen, S. Sun, S.J.H. Ong, S. Xi, C. Diao, Y. Du, J.-O. Wang, M.B.H. Breese, S. Li, H. Zhang, Z.J. Xu, Covalency competition dominates the water oxidation structure–activity relationship on spinel oxides, Nat. Catal. 3(7) (2020) 554-563.https://doi.org/10.1038/s41929-020-0465-6.
[15] H. Xu, D. Guan, Exceptional Anisotropic Noncovalent Interactions in Ultrathin Nanorods: The Terminal σ-Hole, ACS Appl. Mater. Interfaces 14(45) (2022) 51190-51199.https://doi.org/10.1021/acsami.2c14041.
[16] H. Xu, D. Guan, L.J.N. Ma, The bio-inspired heterogeneous single-cluster catalyst Ni100–Fe 4 S 4 for enhanced electrochemical CO 2 reduction to CH 4, Nanoscale 15(6) (2023) 2756-2766.https://doi.org/10.1039/D2NR06665C.
[17] D. Guan, H. Xu, Q. Zhang, Y.-C. Huang, C. Shi, Y.-C. Chang, X. Xu, J. Tang, Y. Gu, C.-W. Pao, S.-C. Haw, J.-M. Chen, Z. Hu, M. Ni, Z. Shao, Identifying A Universal Activity Descriptor and a Unifying Mechanism Concept on Perovskite Oxides for Green Hydrogen Production, Adv. Mater. 2305074.https://doi.org/10.1002/adma.202305074.
[18] C. Duan, J. Tong, M. Shang, S. Nikodemski, M. Sanders, S. Ricote, A. Almansoori, R. O'Hayre, Readily processed protonic ceramic fuel cells with high performance at low temperatures, Science 349(6254) (2015) 1321-1326.https://doi.org/10.1126/science.aab3987.
[19] K. Xu, H. Zhang, Y. Xu, F. He, Y. Zhou, Y. Pan, J. Ma, B. Zhao, W. Yuan, Y. Chen, M. Liu, An efficient steam-induced heterostructured air electrode for protonic ceramic electrochemical cells, Adv. Funct. Mater. 32(23) (2022) 2110998.https://doi.org/10.1002/adfm.202110998.
[20] M. Shang, J. Tong, R. O'Hayre, A promising cathode for intermediate temperature protonic ceramic fuel cells: $BaCo_{0.4}Fe_{0.4}Zr_{0.2}O_{3-\delta}$, RSC Adv. 3(36) (2013) 15769-15775.https://doi.org/10.1039/C3RA41828F.
[21] Y. Zhou, W. Zhang, N. Kane, Z. Luo, K. Pei, K. Sasaki, Y. Choi, Y. Chen, D. Ding, M. Liu, An efficient bifunctional air electrode for reversible protonic ceramic electrochemical cells, Adv. Funct. Mater. 31(40) (2021) 2105386.https://doi.org/10.1002/adfm.202105386.
[22] Y. Song, J. Liu, Y. Wang, D. Guan, A. Seong, M. Liang, M.J. Robson, X. Xiong, Z. Zhang, G. Kim, Z. Shao, F. Ciucci, Nanocomposites: a new opportunity for developing highly active and durable bifunctional air electrodes for reversible protonic ceramic cells, Adv. Energy Mater. 11(36) (2021) 2101899.https://doi.org/10.1002/aenm.202101899.
[23] Y. Song, Y. Chen, W. Wang, C. Zhou, Y. Zhong, G. Yang, W. Zhou, M. Liu, Z. Shao, Self-Assembled triple-conducting nanocomposite as a superior protonic ceramic fuel cell cathode, Joule 3(11) (2019) 2842-2853.https://doi.org/10.1016/j.joule.2019.07.004.
[24] H. Ding, W. Wu, C. Jiang, Y. Ding, W. Bian, B. Hu, P. Singh, C.J. Orme, L. Wang, Y. Zhang, D. Ding, Self-sustainable protonic ceramic electrochemical cells using a triple conducting electrode for hydrogen and power production, Nat. Commun. 11(1) (2020) 1907.https://doi.org/10.1038/s41467-020-15677-z.
[25] D. Huan, N. Shi, L. Zhang, W. Tan, Y. Xie, W. Wang, C. Xia, R. Peng, Y. Lu, New, efficient, and reliable air electrode material for proton-conducting reversible solid oxide cells, ACS Appl. Mater. Interfaces 10(2) (2018) 1761-1770.https://doi.org/10.1021/acsami.7b16703.

[26] Z. Wang, W. Yang, S.P. Shafi, L. Bi, Z. Wang, R. Peng, C. Xia, W. Liu, Y. Lu, A high performance cathode for proton conducting solid oxide fuel cells, J. Mater. Chem. A 3(16) (2015) 8405-8412.https://doi.org/10.1039/C5TA00391A.
[27] W. Tang, H. Ding, W. Bian, W. Wu, W. Li, X. Liu, J.Y. Gomez, C.Y. Regalado Vera, M. Zhou, D. Ding, Understanding of A-site deficiency in layered perovskites: promotion of dual reaction kinetics for water oxidation and oxygen reduction in protonic ceramic electrochemical cells, J. Mater. Chem. A 8(29) (2020) 14600-14608.https://doi.org/10.1039/D0TA05137C.
[28] D. Shan, Z. Gong, Y. Wu, L. Miao, K. Dong, W. Liu, A novel $BaCe_{0.5}Fe_{0.3}Bi_{0.2}O_{3-\delta}$ perovskite-type cathode for proton-conducting solid oxide fuel cells, Ceram. Int. 43(4) (2017) 3660-3663.https://doi.org/10.1016/j.ceramint.2016.11.206.
[29] R. Ren, Z. Wang, C. Xu, W. Sun, J. Qiao, D.W. Rooney, K. Sun, Tuning the defects of the triple conducting oxide $BaCo_{0.4}Fe_{0.4}Zr_{0.1}Y_{0.1}O_{3-\delta}$ perovskite toward enhanced cathode activity of protonic ceramic fuel cells, J. Mater. Chem. A 7(31) (2019) 18365-18372.https://doi.org/10.1039/C9TA04335G.
[30] C. Sun, Y. Li, X. Ye, Z. Wen, A robust air electrode supported proton-conducting reversible solid oxide cells prepared by low temperature co-sintering, J. Power Sources 492 (2021) 229602.https://doi.org/10.1016/j.jpowsour.2021.229602.
[31] F. He, D. Song, R. Peng, G. Meng, S. Yang, Electrode performance and analysis of reversible solid oxide fuel cells with proton conducting electrolyte of $BaCe_{0.5}Zr_{0.3}Y_{0.2}O_{3-\delta}$, J. Power Sources 195(11) (2010) 3359-3364.https://doi.org/10.1016/j.jpowsour.2009.12.079.
[32] E. Vøllestad, R. Strandbakke, M. Tarach, D. Catalán-Martínez, M.-L. Fontaine, D. Beeaff, D.R. Clark, J.M. Serra, T. Norby, Mixed proton and electron conducting double perovskite anodes for stable and efficient tubular proton ceramic electrolysers, Nat. Mater. 18(7) (2019) 752-759.https://doi.org/10.1038/s41563-019-0388-2.
[33] W. Li, B. Guan, L. Ma, S. Hu, N. Zhang, X. Liu, High performing triple-conductive $Pr_2NiO_{4+\delta}$ anode for proton-conducting steam solid oxide electrolysis cell, J. Mater. Chem. A 6(37) (2018) 18057-18066.https://doi.org/10.1039/C8TA04018D.